

# Computing the elastic mechanical properties of rod-like DNA nanostructures

Hemani Chhabra,<sup>†</sup> Garima Mishra,<sup>‡</sup> Yijing Cao,<sup>†</sup> Domen Prešern,<sup>†</sup> Enrico Skoruppa,<sup>¶</sup> Maxime M. C. Tortora,<sup>†,§</sup> and Jonathan P. K. Doye<sup>\*,†</sup>

<sup>†</sup>*Physical & Theoretical Chemistry Laboratory, Department of Chemistry, University of Oxford, South Parks Road, Oxford OX1 3QZ, United Kingdom*

<sup>‡</sup>*Department of Physics, Indian Institute of Technology Kanpur, Kanpur 208016, India*

<sup>¶</sup>*Laboratory for Soft Matter and Biophysics, KU Leuven, Celestijnenlaan 200D, 3001 Leuven, Belgium*

<sup>§</sup>*Laboratory of Biology and Modeling of the Cell, École Normale Supérieure de Lyon, 46, allée d'Italie, 69364 Lyon Cedex 07, France*

E-mail: jonathan.doye@chem.ox.ac.uk

## Abstract

To study the elastic properties of rod-like DNA nanostructures, we perform long simulations of these structure using the oxDNA coarse-grained model. By analysing the fluctuations in these trajectories we obtain estimates of the bend and twist persistence lengths, and the underlying bend and twist elastic moduli and couplings between them. Only on length scales beyond those associated with the spacings between the interhelix crossovers do the bending fluctuations behave like those of a worm-like chain. The obtained bending persistence lengths are much larger than that for double-stranded DNA and increase non-linearly with the number of helices, whereas the twist moduli increase approximately linearly. To within the numerical error in our data, the twist-bend coupling constants are of order zero. That the bending persistence lengths we

obtain are generally somewhat higher than in experiment probably reflects both that the simulated origami have no assembly defects and that the oxDNA extensional modulus for double-stranded DNA is too large.

## 1 Introduction

DNA nanotechnology exploits the programmability of DNA and its ability to self assemble to make nanoscale structures and devices. This is perhaps most famously achieved through the DNA origami approach, where a long single-stranded scaffold can be folded up into almost any arbitrary shape made up of arrays of double helices by the addition of the appropriate short staple strands.<sup>1</sup> Similar scaffold-free approaches where the size of the object is not constrained by the scaffold length are also available.<sup>2-4</sup> Although a huge variety of structures have been produced by these techniques,<sup>5,6</sup> one of the most common classes of structures have been DNA rods or filaments;<sup>7</sup> these are the subject of the current paper.

Understandably, much of the characterization of DNA origami and other large DNA nano-assemblies initially focused on their structure. Cryo-electron microscopy, for example, has revealed the detailed structure of DNA origami in exquisite detail.<sup>8</sup> More recently there has been an increasing interest in characterizing their mechanical properties. One reason is the advent of “DNA mechanotechnology”, that is the use of DNA nanodevices to generate, transmit and sense nanoscale forces.<sup>9</sup> These include examples where DNA nanostructures are used as the “hardware for single-molecule investigations”.<sup>10</sup> For example, in force spectroscopy, rod-like origami have been used as stiff handles for force application with molecular tweezers,<sup>11,12</sup> and small origami have been used to create multivalent force sensors.<sup>13</sup> Origami with inbuilt tension in components have been used to apply forces to unravel protein-DNA complexes<sup>14,15</sup> and to study the force-dependent binding of proteins to DNA motifs.<sup>16,17</sup> Protein-protein interactions have also been measured by the shape changes they induce in an origami to which they are attached.<sup>18</sup> Similarly, origami sensors have been designed that produce a change in FRET signal when interactions are sufficiently strong to induce a shape

change.<sup>19</sup>

For the above applications, it is important to have a good understanding of the mechanical properties of the DNA origami; for example, knowing the stiffness of the origami handles, knowing the compliance of the origamis with respect to the internal forces that they are seeking to apply, being able to accurately calibrate the magnitude of the forces that are being applied, knowing the limits of the forces that can be applied whilst maintaining the structural integrity of the origami.

Designing internal stresses into an origami also provides a means to further control its structure. For example, twisting and bending of origami can be achieved by changing the numbers of base pairs between junctions from their ideal values.<sup>20</sup> Another approach is to use the tension in extended single stranded sections; for example, to maintain the global shape in origami tensegrity structures,<sup>21</sup> and to induce bending in the main body of an origami.<sup>21–23</sup> Bistable DNA origami have also been designed where transitions between the two free-energy minima require bending of the different origami sections.<sup>24</sup> In the above examples, the elastic moduli for bending and twisting of the origami will control the resulting degree of bending or twisting, and the size of the free-energy barrier in the bistable system.

Understanding the mechanical properties of DNA origami is also of fundamental interest. How does the coupling of the DNA double-helical elements lead to the net mechanical behaviour of the origami? How can it be tuned or controlled? The answers to these questions build on our fundamental understanding of the mechanics of double-stranded and single-stranded DNA, which has been revealed in detail through single-molecule experiments, for example using optical and magnetic tweezers to pull and twist DNA,<sup>25</sup> and further analysed theoretically<sup>26</sup> and in simulations.<sup>27,28</sup>

The most basic mechanical properties of DNA nanostructure that we might wish to understand are their elastic moduli. The quantity that has been most commonly probed in experiments is the bending persistence length of elongated origami, particularly of DNA nanotubes. This has been done for origami that are four-, six-, eight- and ten-helix bundles,<sup>11,21,29–31</sup>

single-stranded-tile nanotubes with from five to ten helices<sup>32</sup> and nanotubes made from double-crossover<sup>33,34</sup> or other<sup>35</sup> larger tiles, as well as more open wireframe origami.<sup>36,37</sup> The experimental approaches used include analyses of their molecular contours when adsorbed on surfaces (either through their end-to-end distances<sup>11,30,31,34,35</sup> or from an analysis of their tangent-tangent correlation function<sup>21,32</sup>), their cyclization rates<sup>33</sup> and their force response in magnetic tweezers.<sup>29</sup> For example, the values of the persistence length obtained are in the ranges 740 nm–1  $\mu$ m, 1–3  $\mu$ m and 3–8.2  $\mu$ m for four-,<sup>29,31</sup> six-<sup>11,21,29–32,35</sup> and eight-helix<sup>11,32</sup> bundles, respectively. These values are much larger than those for double-stranded DNA ( $\sim$ 50 nm), and show how the coupling of double-helical elements in a DNA assembly can lead to new mechanical behaviours. Persistence lengths have also been measured for origami connected by linkers of varying stiffness.<sup>38</sup> The magnetic tweezer study was also able to measure the twist modulus of DNA origami, finding values of 390 nm and 530 nm for four- and six-helix bundles, respectively.<sup>29</sup> The moduli associated with radial compression of rod-like origamis have also been probed by atomic-force microscopy.<sup>39</sup>

Most explorations of the mechanical limits of DNA origami have focused on the effects of tension typically applied by optical tweezers or an atomic-force microscope.<sup>40–43</sup> These studies have revealed saw-tooth force-extension profiles, where the origamis yield through multiple unravelling events. The buckling of DNA nanotubes under extreme twisting has also been briefly studied.<sup>29</sup>

Modelling has the potential to play an important role in better understanding the mechanics of DNA nanostructures. Firstly, the experimental measurement of mechanical properties can be challenging, so if modelling can provide a means to accurately estimate such properties, this could be extremely useful—particularly as a means to pre-screen a design for the required mechanical properties, and to explore how those properties can be modulated. Secondly, it can enhance our fundamental understanding, particularly as it allows the mechanical and structural responses to stress to be directly related and the relative roles of different factors to be identified. Modelling also allows theories that predict the mechanical

properties of DNA nanostructures from duplex properties to be consistently tested.

Here, the focus is on computing the elastic mechanical properties of DNA nanotubes. To do this, one has to decide at what level of description it is most appropriate to model the DNA. Of course, all-atom models will provide the most detailed structural description, and all-atom calculations of full-size DNA origami have now been performed,<sup>44,45</sup> albeit at considerable computational cost, even estimating the elastic moduli for cuboidal blocks.<sup>44,46</sup> However, the time scales associated with the long length-scale fluctuations of the full-size DNA nanotubes studied here are likely to be prohibitive for all-atom studies. Very short sections of such DNA nanotubes have been studied by all-atom molecular dynamics with estimates of the stretch moduli being obtained from rapid pulling simulations and persistence lengths from bend angle distributions.<sup>47-49</sup> At the other limit are models that consider DNA helices as simple mechanical elements. Such models have been very successful at providing rapid structural predictions of DNA origami structure, including the effects of internal stresses on structure,<sup>50-52</sup> but their application to study mechanical properties has been more limited.<sup>53</sup>

Coarse-grained models at the nucleotide level have a number of attractive features when considering origami mechanics. They are simple enough that simulations can access sufficiently long time scales to characterize the structural fluctuations of origamis, even in the case of high shape anisotropy. Also, coupling of the stress response to internal degrees of freedom, such as base-pair breaking and unstacking at nick sites, can emerge naturally from the model. However, it is important that the model can accurately reproduce the mechanical properties of double-stranded (and in some instances, single-stranded) DNA, as well as other motifs (e.g. nicks and junctions). Here, we use the oxDNA model as it possesses just such features. It provides a good description of the elastic properties of double-stranded DNA (dsDNA), including not only the persistence length and torsional modulus,<sup>54</sup> but also non-trivial features such as twist-bend coupling.<sup>55,56</sup> It also captures well the yielding of dsDNA under tension<sup>27</sup> and twist.<sup>57</sup>

OxDNA has also been shown to provide a very good structural description of DNA origami<sup>54,58-63</sup> and other large DNA nanostructures.<sup>64-66</sup> It has been used to probe the mechanisms of origami failure under tension,<sup>43</sup> and even to explain the origins of phase chirality of cholesteric phases of twisted DNA origami rods in terms of the net chirality of their thermal fluctuations.<sup>67</sup>

The systems that we consider here focus on those for which there are experimental measurements. As such rod-like origamis are often termed helix bundles we label each system as  $n$ HB, where  $n$  is the number of helices. Firstly, we consider the 4HB and 6HB origami of Ref. 29 whose mechanical properties were probed by magnetic tweezers (MT). Secondly, we consider the set of four 6HB origamis whose liquid-crystalline properties were experimentally studied in Ref. 68 and analysed by simulation and theory in Ref. 67. These are labelled by their designed global axial twist ( $2\times$ LH, $1\times$ LH, $1\times$ RH) or lack thereof (S: straight, i.e. untwisted). The persistence length of 6HB-S was measured in Ref. 11. We also consider a 10HB that was also studied in Ref. 68. Finally, we consider 6HB and 8HB systems made from single-stranded tiles (SST) whose mechanical properties were studied in Ref. 32, plus an additional equivalent 4HB example.

## 2 Methods

### 2.1 oxDNA

OxDNA is a nucleotide-level coarse-grained model of DNA,<sup>54,69,70</sup> where each nucleotide is a rigid body that has sites representing the backbone and base. The inter-nucleotide interactions include base stacking, hydrogen-bonding between complementary base pairs, a backbone potential, excluded volume, electrostatic interactions between the charged backbones and cross stacking between diagonally opposite bases in dsDNA. These have been parameterized to reproduce DNA structure, the thermodynamics of hybridization and the mechanical properties of double- and single-stranded DNA. Here, we use the latest version

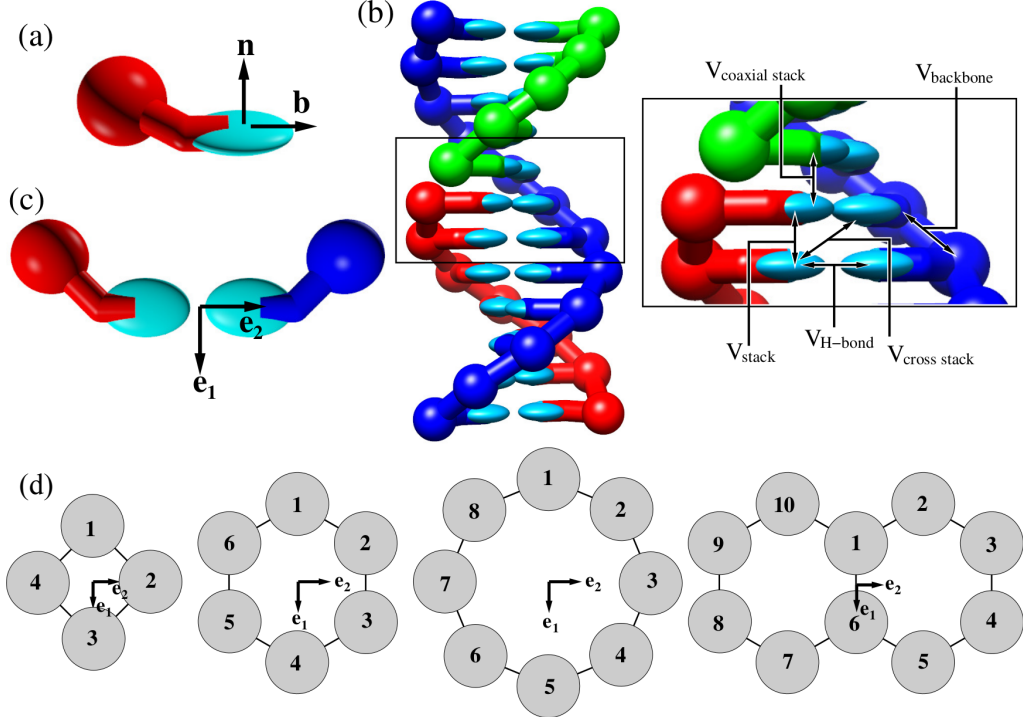


Figure 1: (a) An oxDNA nucleotide along with the “base” and “normal” vectors used to define its orientation. (b) A nicked double helix illustrating the different interactions in oxDNA. (c) An oxDNA base pair illustrating the directions of  $\hat{\mathbf{e}}_1$  and  $\hat{\mathbf{e}}_2$ . (d) Schematics showing  $\hat{\mathbf{e}}_1$  and  $\hat{\mathbf{e}}_2$  for the different DNA nanostructures considered. In (c) and (d)  $\hat{\mathbf{e}}_3$  is directed out of the plane of the paper.

of the model that has been fine-tuned to better reproduce the properties of DNA origami.<sup>54</sup> A nucleotide and duplex as represented by oxDNA are depicted in Fig. 1.

The electrostatic potential is of a Debye-Hückel form and has been fitted to reproduce the  $[\text{Na}^+]$  dependence of hybridization thermodynamics.<sup>54</sup> Here, we have run simulations at  $[\text{Na}^+]=0.5\text{ M}$ , which in oxDNA gives similar behaviour to the high-magnesium conditions typically used in origami assembly. As we are interested in the generic properties of DNA nanotubes, we use the sequence-averaged version of the model, where the interaction strengths of the stacking and hydrogen-bond interactions do not depend on the identity of the base. For DNA origami, the differences between the sequence-averaged model and using the specific M13 sequence are expected to be minimal.

In the oxDNA simulation code the positions and orientations of each nucleotide are defined by  $\mathbf{r}$  the notional centre of mass of the nucleotide (this is collinear with the hydrogen-

bonding and stacking sites),  $\hat{\mathbf{b}}$  the “base” vector (this points from centre of mass towards the base interaction sites), and  $\hat{\mathbf{n}}$  the base normal vector that is perpendicular to the notional plane of the base (Fig. 1(a)). These vectors will be used to define the local bend and twist angles for both a DNA duplex and the DNA nanotubes.

## 2.2 DNA nanotubes

We study the mechanical properties of ten different elongated DNA nanostructures that have been studied experimentally in three separate papers,<sup>29,32,68</sup> focussing mainly on systems where some mechanical properties have been experimentally estimated. Seven of these are DNA origami. In a DNA origami, there is a single long “scaffold” strand that runs through the entire structure, and is held together by many “staple” strands that bind specifically to multiple domains of the scaffold. The scaffold strands in origami typically derive from the genome of an M13 virus, which is just over 7000 nucleotides long. The remaining three DNA nanostructures are structurally very similar, but are made up of just a small number of short DNA strands (or single-stranded tiles<sup>2</sup>) with a repeating motif along the length of the tube.

All the structures are helix bundles, i.e. they are made up of parallel arrays of double helices. The points at which strands pass between helices are termed crossovers or junctions. In the DNA origamis these are typically “double” crossovers where two strands pass between the helices at the junctions, and the ends of the staple strands occur between junctions. By contrast, in the SST nanotubes, the junctions are all “single” crossovers as the ends of the strands are located at the junctions (Fig. 2(a)).

Non-planar DNA origami designs are typically based on either a hexagonal or square lattice of DNA helices, where crossovers occur between adjacent helices of the lattice, and the spacings between junctions are chosen to best match the pitch of DNA (e.g. the junctions are separated by seven base pairs in the hexagonal lattice giving an angle of exactly  $4\pi/3$  between consecutive junction if the pitch of DNA is 10.5 base pairs per turn). The six-helix bundles origamis are based on the hexagonal lattice, and the four-helix bundles on the square



lattice.

For the SST nanotubes, junctions are alternatively spaced 10 and then 11 base pairs apart. For a flat sheet with this design, one might expect that they would be flat and untwisted, as the average crossover spacing matches the DNA pitch. However, as adjacent crossovers involve opposing strands, the groove structure of DNA origami also needs to be considered, and it has been suggested that this leads to a natural curvature.<sup>2</sup> Even with this curvature, rolling up the sheets into tubes will likely introduce stress into the tubes, as the interhelix angles will no longer match their relaxed angles. We choose to study the tube isomer consistent with the presumed natural curvature, where the major groove is on the outside of the tube at the junctions.

The 10HB origami is the only system considered that is not a tube. Instead, it has a double hexagon cross-section (Fig. 1(d)). The anisotropy of the cross-section is expected to lead to substantial differences in the two bending moduli. The 4HB-MT and 6HB-MT origami are also slightly different from the rest in that they have wider blocks at each end of the origami (Fig. S1) to facilitate attachment to the beads in the magnetic tweezer experiments that were performed on them.

Snapshots of example origami and SST nanotubes are given in Fig. 2, with snapshots of some of the remaining systems given in Figs. S1–S3. These illustrate the typical scale of the bending fluctuations in these systems. The differences in the nature of the junctions for these two types of system should also be evident from the close ups.

## 2.3 Simulations

We use molecular dynamics to generate a large ensemble of thermalized configurations of the DNA nanotubes that can then be analysed using the methods described in the subsequent sections to extract persistence lengths and elastic moduli. Our molecular dynamics approach uses an Andersen-like thermostat,<sup>71</sup> both to set the temperature and to generate diffusive motion as is appropriate for nucleotides in solution. Simulations were run at a temperature of

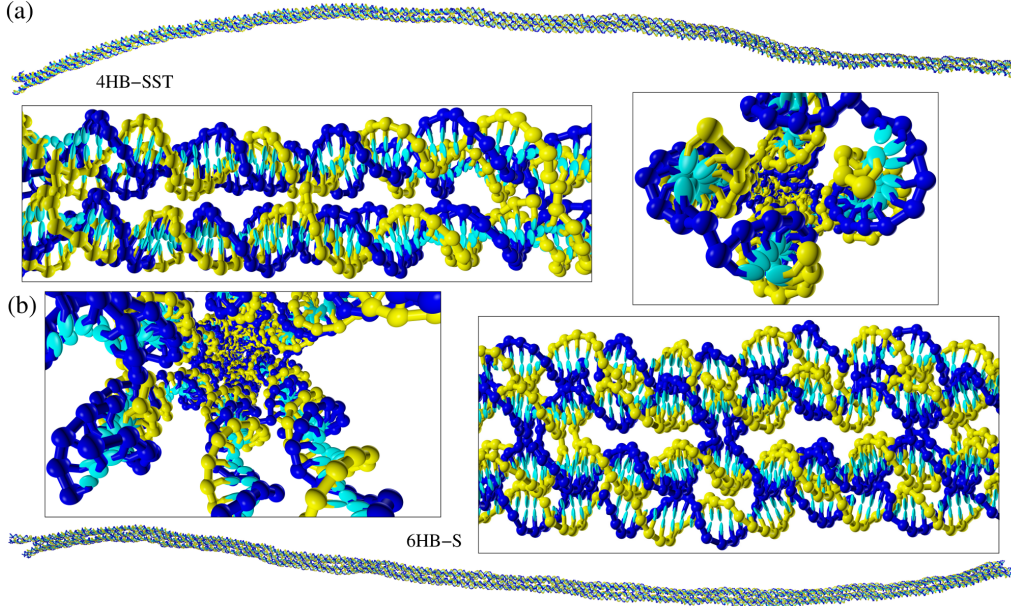


Figure 2: Snapshots of two of the DNA nanostructures (a) 4HB-SST; (b) 6HB-S, including close-ups from the ends and the side.

20 or 23°C. To generate an equilibrium ensemble that samples the large length-scale bending fluctuations well requires very long simulations (the total length of the simulations for each system are between 3 and 18 ms (Table S1)). We monitor the sampling by following the distance between points near the opposite ends of the nanotubes as a function of time (see Fig. S4 for examples). The fastest equilibration occurs for the SST nanotubes. The reason for the somewhat slower dynamics for the origamis is not obvious. The main structural difference in the origamis is that the junctions involve mainly double rather than single crossovers, and so there may be some coupling of bending to different internal geometric states of these junctions that leads to the slower dynamics of the bending fluctuations. The slowest dynamics are for the 4HB-MT and 6HB-MT origamis where the blocks at the end of the origami perhaps slow down the diffusive dynamics of the long length-scale fluctuations. Consequently, these two systems have the worst statistics, which in turn impacts the precision of the computed elastic properties. Further details of the simulations are given in the Supporting Information (Section S2).

## 2.4 Elastic model

The conformation of a stiff polymer can be described by an orthonormal reference frame  $\{\hat{\mathbf{e}}_1(s), \hat{\mathbf{e}}_2(s), \hat{\mathbf{e}}_3(s)\}$  as a function of the arc length  $s$  along the molecular contour, where  $\hat{\mathbf{e}}_3(s)$  is tangential to the contour. For a DNA duplex or nanotube it is natural to discretize a configuration into steps along the contour. For the duplex a natural step is between consecutive base pairs. Similarly, the nanotubes considered here can be divided up into well-defined “slices” transverse to the contour, where each helix of the bundle has a base pair in each slice, and a step corresponds to moving one base pair along each helix. The junctions that interconnect the helices maintain the registry between the base pairs in each slice. Note that, unlike for the duplex, the slices are not all strictly equivalent because of their different positions relative to the junctions.

A rotation vector  $\Theta^{(n)}$  can be defined that represents the rotation of the triad  $\{\hat{\mathbf{e}}_1(n), \hat{\mathbf{e}}_2(n), \hat{\mathbf{e}}_3(n)\}$  onto the adjacent triad  $\{\hat{\mathbf{e}}_1(n+1), \hat{\mathbf{e}}_2(n+1), \hat{\mathbf{e}}_3(n+1)\}$ .<sup>56</sup> The components  $\Theta_1$  and  $\Theta_2$  represent local bending, whereas  $\Theta_3$  is a twist angle about the system axis. If the system is on average straight then one would expect  $\langle \Theta_1 \rangle = \langle \Theta_2 \rangle = 0$ . If we define  $\Omega_i = (\Theta_i - \langle \Theta_i \rangle)/a$ , where  $a$  is the average separation of successive steps, then the harmonic form of the energy due to angular deformations is

$$\beta E = \frac{a}{2} \sum_{n=1}^N \sum_{\mu, \nu=1}^3 \Omega_{\mu}^{(n)} M_{\mu\nu} \Omega_{\nu}^{(n)}. \quad (1)$$

These are the dominant terms at small angular deviations, but higher order terms may be relevant for larger deformations.

If there are no couplings between the different angular degrees of freedom, then

$$\mathbf{M} = \begin{pmatrix} A_1 & 0 & 0 \\ 0 & A_2 & 0 \\ 0 & 0 & C \end{pmatrix}, \quad (2)$$

as would be the case if  $\Omega_1$  and  $-\Omega_1$ , and  $\Omega_2$  and  $-\Omega_2$  were equivalent by symmetry. However, in the general case

$$\mathbf{M} = \begin{pmatrix} A_1 & A_{12} & G_1 \\ A_{12} & A_2 & G_2 \\ G_1 & G_2 & C \end{pmatrix}. \quad (3)$$

For duplex DNA, if  $\Omega_2$  describes bending deformations into the grooves of the helix, there is a symmetry with respect to the bending deformation  $\Omega_1$  that implies  $A_{12} = G_1 = 0$ , and  $G_2$ , the twist-bend coupling constant, is the only non-zero off-diagonal element of  $\mathbf{M}$ .<sup>55,72</sup>

For all the origamis we consider, the designs are based either on a hexagonal lattice (6HB) or square lattice (4HB). For a perfectly regular pattern of junctions and staple ends the highest possible  $C_n$  axis for these two lattices would be  $C_3$  or  $C_2$ , respectively. However, if the helix bundles were infinite in length, and ignoring strand ends (the scaffold runs antiparallel in adjacent helices), the tubes could also possess six-fold and four-fold screw axes, respectively. Therefore, the 4HB and 6HB systems have approximate four-fold and six-fold symmetry. The presence of 2-fold axial symmetry implies that  $A_{12} = G_1 = G_2 = 0$ , and 3-fold or higher rotational symmetry also implies that  $A_1 = A_2$ . That the elastic constants do not fully obey the above is likely due to the breaking of the symmetry due to the irregular placement of junctions and strand ends.

By contrast, adjacent helices in the SST nanotubes are not equivalent. The 4HB-, 6HB- and 8HB-SST nanotubes thus have 2-fold, 3-fold and 4-fold symmetry, respectively. (Note that, unlike the origamis, these systems have a perfectly regular pattern of junctions.) Furthermore, because the spacing between junctions alternates between 10 and 11 base pairs, the inter-helix angles also alternate,<sup>2</sup> and so the cross-sections of the tubes are not expected to be on average regular polygons. Therefore,  $A_1$  and  $A_2$  are expected to be different for the 4HB system, but identical for the larger tubes, whereas one would expect  $A_{12} = G_1 = G_2 = 0$  for all SST systems.

## 2.5 Persistence lengths and elastic moduli

If a system behaves like an ideal worm-like chain, one expects

$$\langle \hat{\mathbf{e}}_3(n) \cdot \hat{\mathbf{e}}_3(n+m) \rangle = \langle \cos \theta(m) \rangle = e^{-ma/l_b}, \quad (4)$$

where  $l_b$  is the bending persistence length and the averaging is performed over both different origins  $n$  and different configurations. Rearranging allows an  $m$ -dependent persistence length to be defined:

$$l_b(m) = -\frac{ma}{\log \langle \cos \theta(m) \rangle}. \quad (5)$$

Note that, as the number of possible origins is fewer for larger  $m$ , and the longest length scale fluctuations will be least well sampled in the simulations, the statistical errors are expected to increase with  $m$ . Similarly, one can define a twist persistence length in terms of the decay of the cumulative twist angle deviation

$$l_t(m) = -\frac{ma}{\log \langle \cos \left( \sum_{k=n}^{n+m-1} a \Omega_3^{(k)} \right) \rangle}. \quad (6)$$

To compute the elastic constant matrix  $\mathbf{M}$  we use the same approach as was used for DNA duplexes in Ref. 56. Namely, we first calculate the correlation matrix  $\Xi$  which is defined below

$$\Xi_{\mu\nu}(m) = \left\langle \left[ \sum_{k=n}^{n+m-1} \Omega_\mu^{(k)} \right] \left[ \sum_{l=n}^{n+m-1} \Omega_\nu^{(l)} \right] \right\rangle. \quad (7)$$

Inversion of  $\Xi$  leads to the elastic constant matrix:

$$\mathbf{M}(m) = \frac{m}{a} [\Xi(m)]^{-1}. \quad (8)$$

The use of cumulative angular deformations in Eq. 7 is discussed further in Ref. 73.

Note that the local form of the elastic energy in Eq. 1 would imply that the persistence lengths and elastic moduli are independent of  $m$ . In practice, however, there are longer-range

effective couplings that lead to a variation with  $m$ , where convergence to a constant value only emerges at larger  $m$ , as has previously been observed for the DNA duplex.<sup>56</sup> Here, we are most interested in this asymptotic behaviour, as it describes the long length-scale bending and twisting fluctuations.

Another implication of Eq. 1 is that the probability distributions for  $\Omega_i$  would be expected to be Gaussian. These distributions are illustrated in Figs. S5(a)-S8(a) for the 4HB-MT, 6HB-MT and 6HB-SST systems. For the 6HB-SST nanotube, the  $\Omega_i$  distributions show some deviations from Gaussianity with large angular deformations being somewhat more likely than would be expected. By contrast, the two origami have much more significant deviations in the tails of these distributions, with the 6HB-MT origami showing clear sub-peaks in the distributions for the bending deformations. It might be that these more extreme local fluctuations are related to the slower dynamics of the origamis which were previously noted in Section 2.3. Figs. S5-S8 also show the distributions for the cumulative angular deformations used in Eq. 7 for different values of  $m$ . As expected,<sup>74</sup> these distributions converge to a Gaussian form as  $m$  increases, with this convergence occurring more rapidly for the 6HB-SST nanotube. Thus, although there are deviations from worm-like chain behaviour at the level of a single step, on longer renormalised length scales worm-like chain statistics apply.

When applying the above formulae to a DNA duplex or the DNA nanotubes, we choose to not include a certain number of base pairs or tube slices at either end, as the ends will typically be somewhat more flexible. In the nanotubes, this general effect is exacerbated by the significant structural differences at the ends. The helices splay out much more at the ends due to the lack of constraining junctions, as is evident from the snapshots in Fig. 2. The number of tube slices at each end that are ignored is given in Table S1 for each system.

## 2.6 Triad definitions

In Ref. 56 a number of different triads were considered when analysing the elastic properties of the DNA duplex. Here, we recap the definitions for their “Triad III”, as this approach will be most naturally adapted to the DNA nanotubes. In this triad, the positions of the centres of mass of the base pairs are used to define the vector  $\hat{\mathbf{e}}_3$ . Namely,

$$\hat{\mathbf{e}}_3(i) = \frac{\mathbf{R}_{\text{duplex}}(i+1) - \mathbf{R}_{\text{duplex}}(i-1)}{\|\mathbf{R}_{\text{duplex}}(i+1) - \mathbf{R}_{\text{duplex}}(i-1)\|} \quad (9)$$

where  $\mathbf{R}_{\text{duplex}}$  is given by:

$$\mathbf{R}_{\text{duplex}} = \frac{\mathbf{r}_{\text{nuc1}} + \mathbf{r}_{\text{nuc2}}}{2}. \quad (10)$$

The vector between the centres of mass of the nucleotides in the base pair is used to define  $\hat{\mathbf{y}}$

$$\hat{\mathbf{y}} = \frac{\mathbf{r}_{\text{nuc1}} - \mathbf{r}_{\text{nuc2}}}{\|\mathbf{r}_{\text{nuc1}} - \mathbf{r}_{\text{nuc2}}\|} \quad (11)$$

whose orthonormalization with respect to  $\hat{\mathbf{e}}_3$  leads to  $\hat{\mathbf{e}}_2$ :

$$\hat{\mathbf{e}}_2 = \frac{\hat{\mathbf{y}} - (\hat{\mathbf{y}} \cdot \hat{\mathbf{e}}_3) \hat{\mathbf{e}}_3}{\|\hat{\mathbf{y}} - (\hat{\mathbf{y}} \cdot \hat{\mathbf{e}}_3) \hat{\mathbf{e}}_3\|} \quad (12)$$

Finally,  $\hat{\mathbf{e}}_1$  follows from the cross product:

$$\hat{\mathbf{e}}_1 = \hat{\mathbf{e}}_2 \times \hat{\mathbf{e}}_3. \quad (13)$$

The results for  $l_b(m)$  using this triad show an oscillation on the length scale of the pitch length of DNA that dies away at large  $m$  (Fig. 3(a)). Also,  $\langle \Theta_2 \rangle$  was found to have a non-zero value (Fig. 3(b)).<sup>56</sup> The reason is that  $\mathbf{R}_{\text{duplex}}$  does not exactly lie at the centre of the DNA double helix, but is slightly displaced towards the minor groove. Thus, the line of base-pair centres will be helical, and the correlations in  $\hat{\mathbf{e}}_3$  will be strongest for an integer multiple of the pitch length. Similarly, the helicity measure introduced in Ref. 67 when

applied to the contour defined by  $\mathbf{R}_{\text{duplex}}$  shows a sharp peak at the reciprocal of the pitch length (Fig. 3(c)). (Note, the helicity measure has magnitude one for a perfect helix, and positive/negative values correspond to right-handed/left-handed helicity, respectively.)

Although the above oscillation is not problematic for computing  $l_b$  for duplex DNA as the oscillation dies away and the bulk limit is reached on reasonable length scales, when performing a similar analysis for the DNA nanotubes, the issue is much more troublesome. If we define, the centre of the DNA nanotube as the average over the centres of mass of the duplexes in a given slice:

$$\mathbf{R}_{\text{tube}} = \frac{1}{N_{\text{helix}}} \sum_{j=1}^{N_{\text{helix}}} \mathbf{R}_{\text{duplex},j} \quad (14)$$

and  $\hat{\mathbf{e}}_3(i)$  in an analogous manner to the duplex

$$\hat{\mathbf{e}}_3(i) = \hat{\mathbf{z}}(i) = \frac{\mathbf{R}_{\text{tube}}(i+1) - \mathbf{R}_{\text{tube}}(i-1)}{\|\mathbf{R}_{\text{tube}}(i+1) - \mathbf{R}_{\text{tube}}(i-1)\|} \quad (15)$$

the persistence length can be calculated using Eq. 5, as illustrated for one of the origami six-helix bundles in Fig. 3(d). The magnitude of the oscillation on the pitch length is much stronger and persists over the whole range of  $m$  that can be sampled. This is for two reasons. Firstly, the helices in the nanotubes are held in registry by the four-way junctions present in the origamis, and so the helical paths of the centrelines of the individual helices in the nanotubes add up coherently. Secondly, the helix bundles are much stiffer than a DNA duplex and so the variations in the tangent-tangent correlation function due to the helicity of the centerline both make a much more significant contribution and do not significantly die away because the persistence length of the tubes is much longer than the contour length of the nanotubes. Unlike for duplex DNA, a similar oscillation is also seen in the bending elastic constants calculated using Eq. 8 (Fig. S8). Interestingly, for the SST nanotubes no pitch-length oscillation is observed, presumably because the single-crossover junctions place fewer constraints on the relative orientations of adjacent helices, leading to a loss of coherence between the twist of the individual helices (Fig. S8).



In Ref. 75, an approach to correct for the helicity of the duplex contour was introduced that involved transforming from the helical frame of reference to a non-helical one; this transformation led to a small correction to the elastic moduli. Here, we explore an alternative approach that will be more convenient for the DNA nanotubes and instead uses a new definition of the duplex centre  $\mathbf{R}_{\text{duplex}}$  that attempts to remove the helicity by adding a small offset in the direction of the major groove. Namely,

$$\mathbf{R}_{\text{duplex}}(\alpha) = \frac{\mathbf{r}_{\text{nuc1}} + \mathbf{r}_{\text{nuc2}}}{2} + \frac{\alpha}{2} \left( \hat{\mathbf{b}}_{\text{nuc1}} \times \hat{\mathbf{n}}_{\text{nuc1}} + \hat{\mathbf{b}}_{\text{nuc2}} \times \hat{\mathbf{n}}_{\text{nuc2}} \right) \quad (16)$$

where for  $\alpha = 0$  the original definition of Eq. 10 is recovered.

Using this new definition of  $\mathbf{R}_{\text{duplex}}(\alpha)$  in Eq. 9, the oscillation in  $l_b(m)$  is reduced as  $\alpha$  is increased until the oscillation disappears at  $\alpha = 0.06$  (Fig. 3(a)). Similarly, if we examine  $\langle \Theta_2(\alpha) \rangle$ , it passes through zero at  $\alpha = 0.06$  (Fig. 3(b)). Furthermore, the peak in the helicity measure at the reciprocal of the pitch length disappears for  $\alpha = 0.06$  (Fig. 3(c)). Although the value of  $\alpha$  does not affect the limiting value of the bending persistence length for the duplex, it does lead to small changes in the elastic constants, as was also found when switching to a non-helical frame of reference.<sup>75</sup> The variation of the duplex elastic constants with  $\alpha$  is shown in Fig. S9.

Applying the new definition of the duplex centre with  $\alpha = 0.06$  to the origami nanotubes leads to the removal of the oscillations in  $l_b(m)$  (Fig. 3(d)). Note that the  $\alpha = 0.06$  line for  $l_b(m)$  is an upper envelope function to the curves for other values of  $\alpha$ , because the helicity of the centerline leads to a periodic loss in correlations that is not representative of the true stiffness of the system. For all further results we will use  $\alpha = 0.06$ .

Now having a non-helical definition of the tube centre, we consider our definitions of  $\hat{\mathbf{e}}_1$  and  $\hat{\mathbf{e}}_2$ . Following the recipe of Triad III for the duplex, we could define  $\hat{\mathbf{y}}$  for a six-helix bundle as

$$\hat{\mathbf{y}} = \frac{\mathbf{R}_{\text{duplex}}(2) + \mathbf{R}_{\text{duplex}}(3) - \mathbf{R}_{\text{duplex}}(5) - \mathbf{R}_{\text{duplex}}(6)}{\|\mathbf{R}_{\text{duplex}}(2) + \mathbf{R}_{\text{duplex}}(3) - \mathbf{R}_{\text{duplex}}(5) - \mathbf{R}_{\text{duplex}}(6)\|} \quad (17)$$

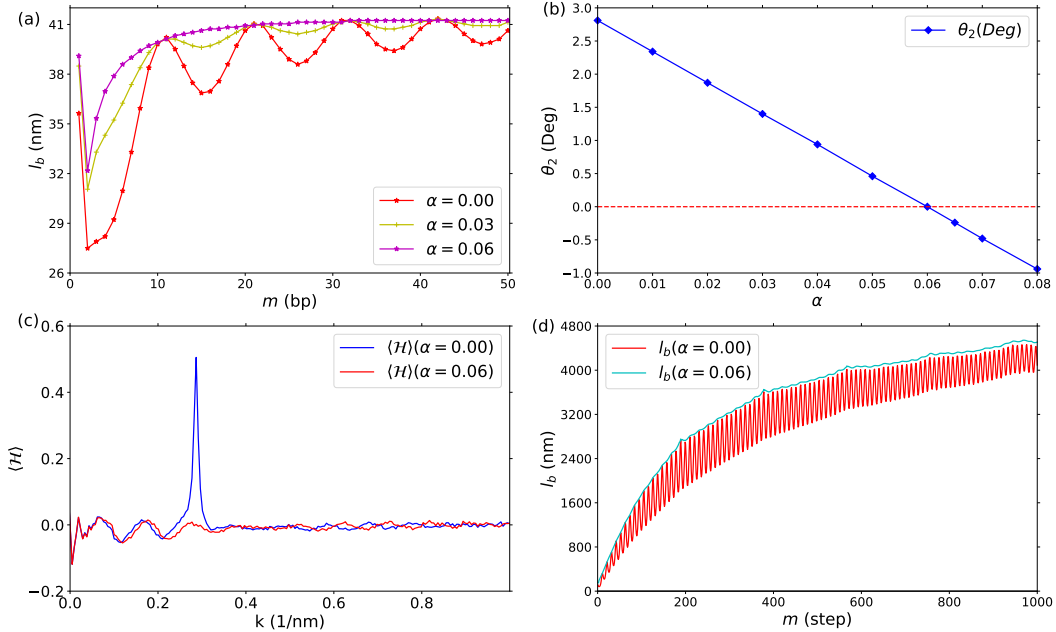


Figure 3:  $l_b(m)$  for (a) dsDNA and (d) the 6HB-S origami at different values of  $\alpha$ , as labelled. (b)  $\langle \Theta_2 \rangle$  for dsDNA as a function of  $\alpha$ . (c) Helicity measure for dsDNA as a function of inverse wavelength at  $\alpha = 0$  and 0.06.

and then use Equations 12 and 13 to obtain  $\hat{\mathbf{e}}_1$  and  $\hat{\mathbf{e}}_2$ . However, when we did so for the 6HB-SST system we found that  $A_1 > A_2$  (Fig. S10(a)) in contrast to our expectations based on the symmetry of the system. We suspected this may be because of the “inequitable” treatment of the three directions in the orthogonalization scheme.

As a test we therefore defined

$$\hat{\mathbf{x}} = \frac{\mathbf{R}_{\text{duplex}}(4) - \mathbf{R}_{\text{duplex}}(1)}{\|\mathbf{R}_{\text{duplex}}(4) - \mathbf{R}_{\text{duplex}}(1)\|}, \quad (18)$$

obtained  $\hat{\mathbf{e}}_1$  by orthogonalization of  $\hat{\mathbf{x}}$  to  $\hat{\mathbf{e}}_3$ , and  $\hat{\mathbf{e}}_2$  by the vector product of  $\hat{\mathbf{e}}_3$  and  $\hat{\mathbf{e}}_1$ . With this scheme the order of the bending moduli was reversed with  $A_2 > A_1$  (Fig. S10(b)), showing this not to be a property of the tube but a reflection of the order in which we performed the orthogonalization.

Therefore, we instead explored using singular value decomposition to find the orthogonal set  $\{\hat{\mathbf{e}}_1, \hat{\mathbf{e}}_2, \hat{\mathbf{e}}_3\}$  that are closest to the set of vectors  $\{\hat{\mathbf{x}}, \hat{\mathbf{y}}, \hat{\mathbf{z}}\}$ .<sup>76</sup> As one can see from Fig. 4,

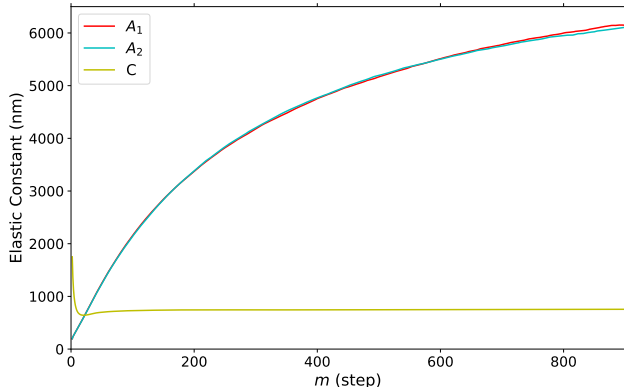


Figure 4: Elastic moduli for 6HB-SST using singular value decomposition.  $\alpha = 0.06$ .

for the 6HB-SST system, within the statistical errors, there is now essentially no difference between  $A_1$  and  $A_2$ , in line with our expectations based on the symmetry of these nanotubes. For the 8HB-SST, this is also true (Fig. S24(c)). Note that for the origamis, the non-regular pattern of junctions is one factor that can somewhat break this potential symmetry. For all further results we use the singular value decomposition approach.

The definitions of  $\hat{\mathbf{x}}$  and  $\hat{\mathbf{y}}$  for the other systems are given in the Supporting Information (Section S3.2) and illustrated on the tube cross-sections in Fig. 1(d). All the definitions that we have introduced are designed for DNA that adopts a base-paired double-helical configuration. However, for structures as large as DNA origamis, there will always be some designed base-pairs that are not intact due to thermal fluctuations. These broken base pairs are most likely to be at nicks and junctions. When such “fraying” occurs, it is likely to lead to anomalous values for the angular deviations  $\Omega_i$ . However, we do not attempt to treat such cases differently or exclude them from our averaging, because both fraying is a natural part of the dynamics of the systems and the number of broken base pairs is likely to be a very small fraction of the total number of base pairs.

## 2.7 Extracting limiting values

The  $m$ -dependent definitions of the persistence lengths (Eqs. 5 and 6) and elastic moduli (Eq. 8) both for the duplexes and the nanotubes show a similar behaviour rising up towards

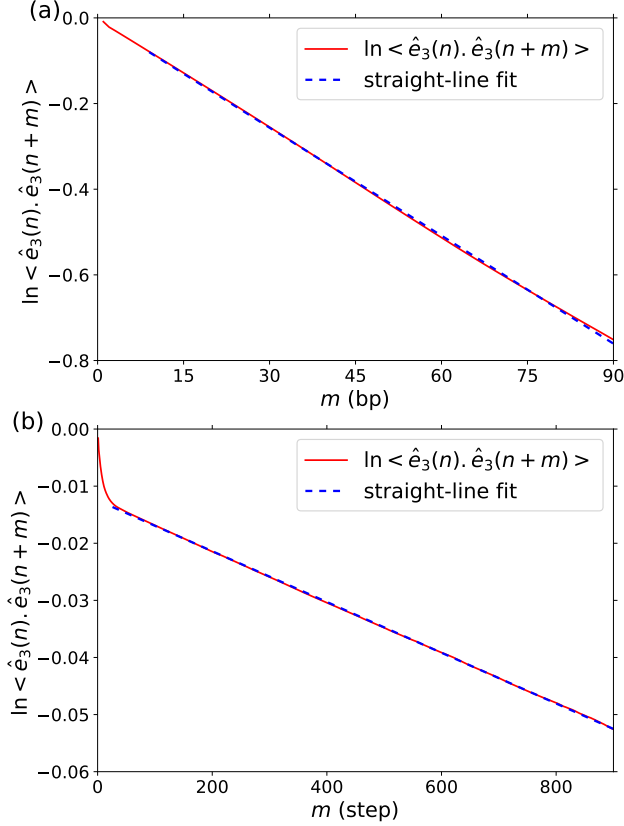


Figure 5:  $\log \langle \cos \theta(m) \rangle$  versus  $m$  for (a) duplex and (b) 6HB-SST along with fit lines to the exponential tail.

a limiting value at large  $m$  (Fig. 3(d) and 4). However, unlike for the duplex, we cannot simply obtain the bulk values of the bending persistence length and the bend elastic moduli from their values at the largest  $m$  value that we sample, because the bending persistence lengths of the nanotubes are much larger than their lengths, and so have not yet converged to their limiting values.

The reason for this strong  $m$ -dependence is that the local fluctuations in the angles  $\Theta_1$  and  $\Theta_2$  are greater than would be expected from the bending of the nanotube contour on long length scales. This effect can be seen in Fig. 5, which depicts the tangent-tangent correlation function. The behaviour is not perfectly exponential, as would be the case for an ideal worm-like chain (Eq. 4), but shows an initial more rapid decay, which for the duplex is only a few base pairs but for the example nanotube is on the order of twenty-five slices.

While for the duplex all base pairs are equivalent, all slices of a nanotube are not equivalent because of their different positions with respect to the junctions. This provides an additional source of heterogeneity that we average over in our analysis. For example, it is well known that the adjacent helices in an origami splay apart slightly as one moves away from the junctions<sup>1,61,77</sup> (Fig. 2) leading to a local bending of the helices that is not representative of their longer-length-scale behaviour.

Fig. 5 suggests a simple way to extract the bulk persistence length. As beyond the transient behaviour at small  $m$  the correlation function shows a near perfectly exponential tail,  $l_b$  can be extracted from the limiting slope of the graph. The same approach is used to calculate  $l_t$  (Fig. S11).

Extracting bulk bending elastic moduli is more difficult. That the fluctuations of  $\Theta_1$  and  $\Theta_2$  are not fully representative of the bending behaviour at long length scales implies that there are correlations beyond a single step. These can be quantified by the following correlation coefficients:

$$\Lambda_{\mu\nu}^{(n)} = \langle \Omega_{\mu}^{(i)} \Omega_{\nu}^{(i+n)} \rangle. \quad (19)$$

In Ref. 73, it has been shown that the matrix  $\Xi(m)$  can be constructed from these correlation coefficients, as follows.

$$\Xi_{\mu\nu}(m) = m\Lambda_{\mu\nu}^{(0)} + \sum_{n=1}^{m-1} (m-n) \left( \Lambda_{\mu\nu}^{(n)} + \Lambda_{\nu\mu}^{(n)} \right). \quad (20)$$

In Fig. S12 we show that the elastic constants obtained from the above formula reproduce well the elastic constants obtained from Eq. 7 for 6HB-SST. However, when we use this approach to extrapolate to larger  $m$ , the behaviour becomes less sensible, and so does not provide a method to estimate the bulk elastic constants. The issue is that the weighting of the longer-range (i.e. larger  $n$ ) correlation coefficients in Eq. 20 becomes more significant at large  $m$ , and although these coefficients might be expected to converge to zero as  $n$  increases, in practice the statistical noise in their values leads to somewhat random behaviour in the

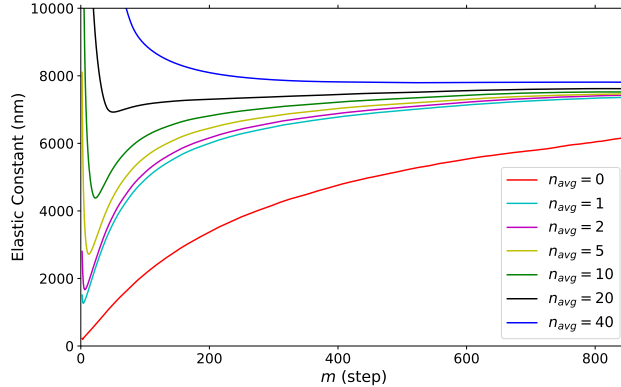


Figure 6: The effect of averaging on  $A_1$  for different  $n_{\text{avg}}$  for the 6HB-SST nanotube.

predicted elastic constants when extrapolating beyond the length of the nanotubes.

Therefore, we have explored an alternative approach in which we perform averaging over longer length scales to reduce the enhanced local fluctuations that are at the root of the issue, and hence to expedite convergence of the elastic moduli to their bulk limit. This idea is similar to using a renormalized length scale; as we noted in Section 2.5 the cumulative angular deformations exhibit behaviour increasingly consistent with worm-like chain statistics as  $m$  increases. We do this averaging by defining our local axes at each slice to be an average of the current slice and  $n_{\text{avg}}$  slices on either side, i.e.

$$\hat{\mathbf{x}}'(i) = \frac{\sum_{j=i-n_{\text{avg}}}^{j=i+n_{\text{avg}}} \hat{\mathbf{x}}(j)}{\left\| \sum_{j=i-n_{\text{avg}}}^{j=i+n_{\text{avg}}} \hat{\mathbf{x}}(j) \right\|} \quad (21)$$

and equivalently for  $\hat{\mathbf{y}}'$  and  $\hat{\mathbf{z}}'$ . As before we then use singular value decomposition to find the  $\hat{\mathbf{e}}_i$  vectors from the triad  $\{\hat{\mathbf{x}}', \hat{\mathbf{y}}', \hat{\mathbf{z}}'\}$ . Fig. 6 illustrates the behaviour of the elastic constant  $A_1$  for the 6HB-SST system for different values of  $n_{\text{avg}}$ . As  $n_{\text{avg}}$  increases, the stiffness at small  $m$  increases quickly, as intended. For sufficiently large  $n_{\text{avg}}$  the  $m$ -dependent elastic moduli even become larger than their bulk values and convergence to the limiting value as  $m$  increases occurs from above. It is also clear from the figure that the curves for different  $n_{\text{avg}}$  are converging to the same limiting value. Therefore, we equate the bulk elastic moduli with their value at large  $m$  (typically at an  $m$  value somewhat lower than the largest we sample

Table 1: Structural and mechanical properties of all the systems studied. All angles are given in degrees and elastic moduli and persistence lengths in nanometres. The  $n_{\text{avg}}$  and  $m_{\text{limit}}$  values used to extract the bulk values of the elastic constants are given in Table S1.

	Ref.	$n_{\text{helix}}$	$N_{\text{slice}}$	$a$	$\langle\Theta_1\rangle$	$\langle\Theta_2\rangle$	$\langle\Theta_3\rangle$	$A_1$	$A_2$	$C$	$l_b$	$l_t/2$	$l_b^{\text{expt}}$	$C_{\text{expt}}$
4HB-MT	29	4	1354	0.3373	0.006	0.010	0.035	2150	2020	330	1040	330	740	390
4HB-SST		4	1029	0.3400	-0.004	0.002	0.136	3120	1750	370	2030	280		
6HB-2×LH	68	6	1259	0.3371	0.002	-0.005	-0.884	4480	5300	610	4500	620		
6HB-1×LH	68	6	1261	0.3376	0.002	-0.003	-0.419	5520	5980	580	5740	680		
6HB-S	68	6	1260	0.3383	-0.001	-0.001	0.046	6400	5780	670	5430	660	2400	
6HB-1×RH	68	6		0.3457	0.004	0.000	0.492	5590	4860	650	5950	690		
6HB-MT	29	6	1085	0.3385	-0.013	-0.011	0.071	6960	5560	800	4140	810	1880	530
6HB-SST	32	6	1070	0.3389	0.000	0.000	0.115	7560	7630	750	7620	740	3300	
8HB-SST	32	8	1050	0.3383	0.000	0.001	0.111	16980	16880	1290	16620	1270	8200	
10HB	68	10	705	0.3379	-0.008	0.002	0.012	37580	13440	2230	19440	1780		

because the latter are most affected by statistical noise; the values used are given in Table S1) when using the value of  $n_{\text{avg}}$  for which convergence is most rapid. Figures equivalent to Fig. 6 but for  $A_2$  and  $C$  are given in the Supporting Information (Fig. S13), along with the effects of this averaging on the persistence length measurements. For example, for the 6HB-SST nanotube we use  $n_{\text{avg}} = 20$  to obtain bulk  $A_1$  and  $A_2$  values, and  $n_{\text{avg}} = 5$  to obtain  $C$  (Table S1).

### 3 Results

A range of structural and mechanical properties of the ten systems that we studied are given in Table 1. Firstly,  $\langle\Theta_1\rangle$  and  $\langle\Theta_2\rangle$  for all systems are zero within statistical error; i.e. all the tubes are on average straight, as expected. The behaviour of  $\langle\Theta_3\rangle$  is more interesting. We should first note that the current oxDNA potential has been fine-tuned to reproduce the experiments of Ref. 20 which suggested that origami based on the hexagonal lattice and without any insertions or deletions should be approximately untwisted. Consistent with this, the 6HB-S, 6HB-MT and 10 HB origami are all fairly near to being untwisted, albeit with all showing a slight right-handed twist; this twist is lowest for the 10HB reflecting its significantly larger twist modulus.

The series of twisted six-helix bundles of Ref. 68 show the expected linear variation of the twist (Fig. S14) across the series, albeit with the nanotube that is designed to be untwisted

being slightly right-handed, as noted above. The designed twist in these structures is based on modelling with CanDo.<sup>50,51</sup> Here, we find that the insertions and deletions (i.e. increasing or decreasing the number of base pairs between these junctions to induce internal twist stress<sup>20</sup>) in these structures have a larger angular effect with 30 sets of insertions or deletions causing a change in twist of just over one and a half turns rather than a single turn.

Interestingly, the single-stranded tiles systems all show significant right-handed twist (equivalent to about 120° degrees per 1000 base pairs). Like for the hexagonal lattice origamis, the average junction spacing in the planar sheets on which they are based matches the presumed pitch length of DNA (10.5 base pairs). Therefore, they might be expected to show a similar twist as those origamis; instead it is over twice as large. This is mostly because the twist angle at a junction with a single-crossover is larger than for one with a double-crossover for the oxDNA model.

Another basic structural property that we considered was the radius of the tubes defined as the average distance of the centres of the DNA helices from the tube centre:

$$r = \frac{1}{N_{\text{helix}}} \sum_{j=1}^{N_{\text{helix}}} |\mathbf{R}_{\text{duplex}}(j) - \mathbf{R}_{\text{tube}}|. \quad (22)$$

Note, to get a measure of the limit of the excluded volume of the tube one should add the radius of the DNA duplex. The dependence of the radius on position along the tube is shown in Fig. 7(a) for 6HB-S; equivalent figures for all the other systems are depicted in Figs. S15–S17 of the Supporting Information. Typical of all systems, the tube has a significantly larger radius at either end. This is simply a reflection of the significant splaying out of the helices of the origami at the ends that is evident from the snapshots in Fig. 2 and is a result of these sections being less constrained by junctions. The radius measurements allows us to decide how many slices from each end to ignore when performing the persistence length and elastic moduli calculations.

The radii are also larger than one would expect from close-packing of the helices. This is



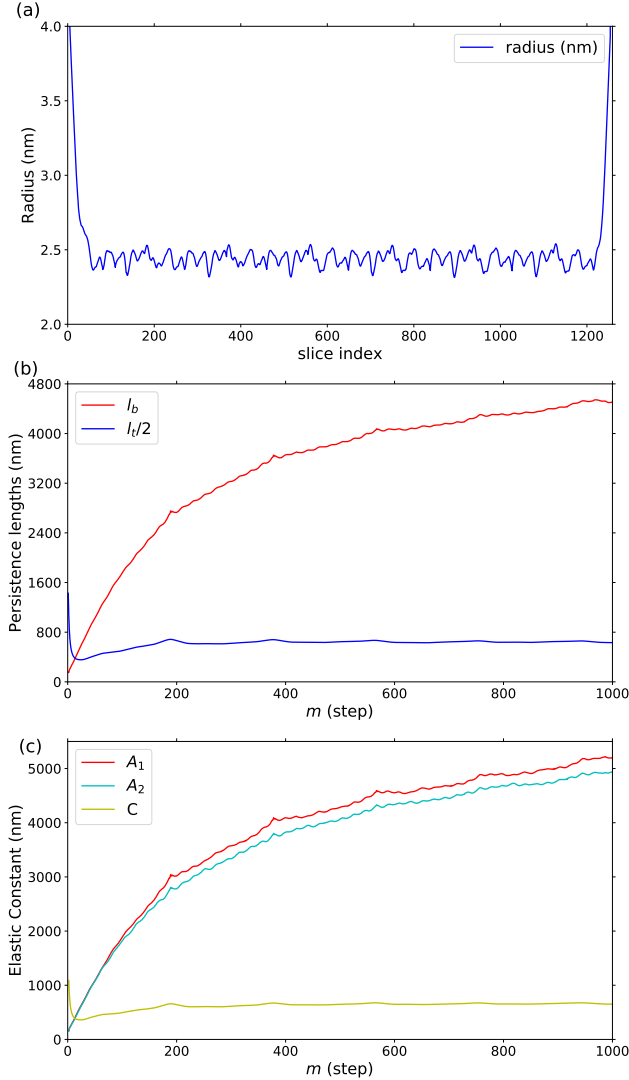


Figure 7: (a) Radius as a function of position, (b)  $m$ -dependent persistence lengths and (c) elastic moduli for the 6HB-S origami.

a result of the well-documented slight splaying out of helices between junctions<sup>1,61,77</sup> that is also visible from the close-ups in Fig. 2. Baker *et al.* estimated the inter-helix separation in a 10-helix bundle nanotube to be 2.75 nm from SAXS measurements.<sup>77</sup> This is fairly similar to the 2.4–2.5 nm radius that we find for the six-helix bundles (Figs. 7(a), S15,S17). The small variations in this radius along the length of the tube are also due to the variations in the interhelix distance caused by this splaying. In the example in Fig. 7(a), the relatively irregular placement of these junctions means there is little clear pattern in this variation, however for the origamis of Ref. 29 there is a much clearer repeating pattern (Fig. S15).

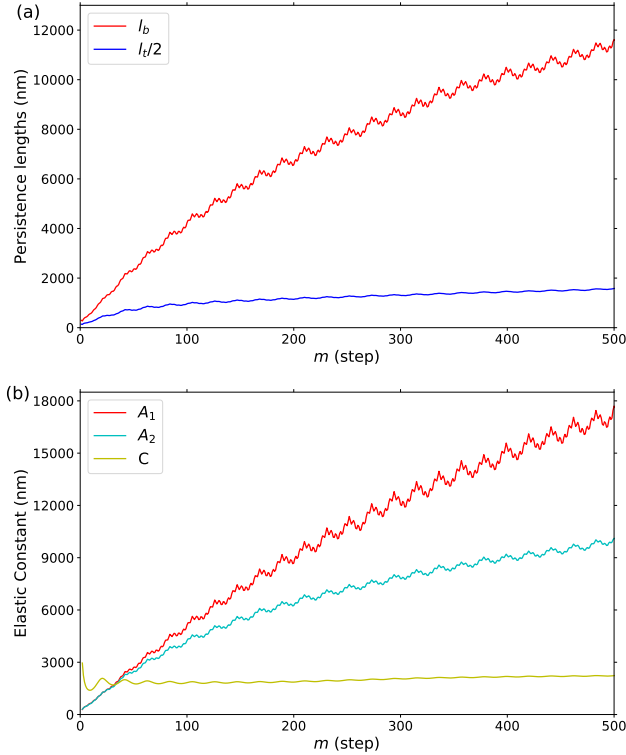


Figure 8: (a)  $m$ -dependent persistence lengths and (b) elastic moduli for the 10HB origami.

The  $m$ -dependent persistence lengths and elastic moduli are shown for 6HB-S, 10HB and 4HB-SST in Figs. 7, 8 and 9, respectively; those for the other systems are shown in Figs. S18–S21. The limiting values of these quantities extrapolated by the approaches outlined in Section 2.7 are given in Table 1 for all systems. As noted already, the  $m$ -dependent bending persistence lengths show a slow convergence to their limiting values due to the enhanced flexibility on short length scales. The twist persistence length, partly reflecting its smaller value, converges much more rapidly. All the origamis show some degree of repetitive fine structure in these curves. For example, there is a small peak every about 190 slices for 6HB-S (Fig. 7(b)) and a stronger oscillation every 21 slices for 10HB (Fig. 8(a)). The enhanced correlations at the peaks are associated with length scales that match a periodicity or approximate periodicity in the pattern of junctions; these periodicities are also evident in the repeating patterns seen in the tube radii. By contrast, the virtual absence of any fine structure, and consequent smoothness of all the data, for the SST nanotubes (e.g. Fig. 9(a))

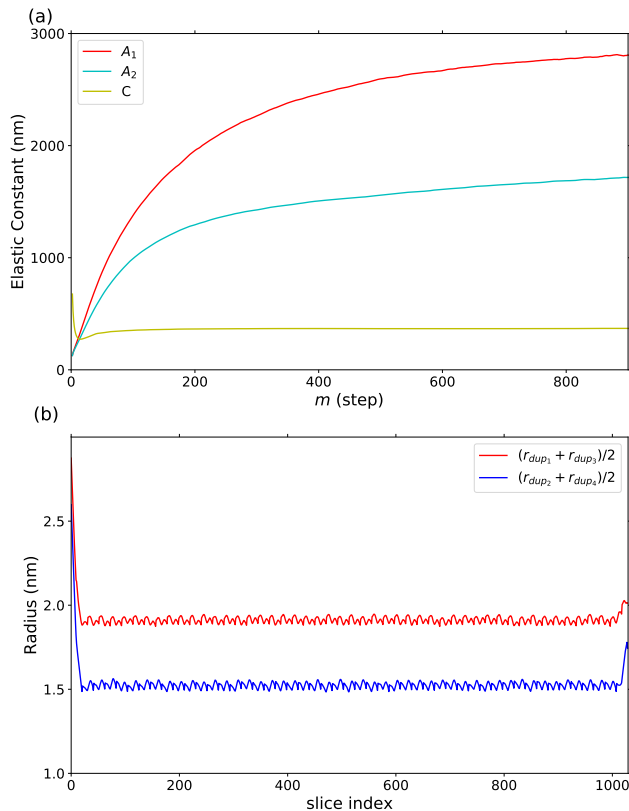


Figure 9: (a)  $m$ -dependent elastic moduli and (b) radii for equivalent helices as a function of position for the 4HB-SST nanotube.

is noteworthy, and reflects the much smaller variations in the tube radii due to the lesser constraints associated with their single-crossover junctions (Fig. 9(b)).

In Fig. 10 we plot the bulk persistence lengths for bending and twisting versus  $n_{\text{helix}}$  for all systems, including dsDNA. There is a clear non-linear increase in the bending persistence length with the number of helices, whereas the twist persistence length increases roughly linearly. For example, the bending persistence lengths of the six-helix bundles are 110–190 times that of dsDNA, whereas the twist persistence length increases only by a factor of 6–9. This basic behaviour was previously noted in Refs. 29 and 32. The variation of the bending persistence length can be described theoretically if one assumes that dsDNA behaves as a uniform elastic cylindrical rod, leading to the expression:<sup>35</sup>

$$l_b^{\text{tube}} = n_{\text{helix}} l_b^{\text{duplex}} \left( 1 + 2 \left( \frac{R}{r} \right)^2 \right). \quad (23)$$

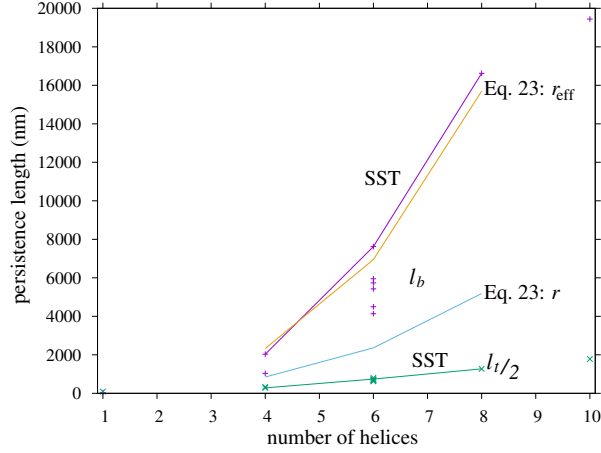


Figure 10: The variation of the bend and twist persistence lengths with  $n_{\text{helix}}$  for all systems including dsDNA. Lines have been added for the SST series of nanotubes. There are also two additional lines (with no data points) that represent the predictions of Eq. 23 for the SST nanotubes using both the actual radius of dsDNA or an effective radius that is chosen to fit the observed data.

where  $r$  is the radius of dsDNA and  $R$  the radius of the nanotube (see Section S4.2). From this equation it can be seen that the non-linear variation is due to the additional effect of the helices being a distance  $R$  from the centreline of the nanotube. One difficulty when applying this to experimental systems is that of measuring  $R$ . However, all quantities in this expression can be measured in simulations, allowing the consistency of this expression to be tested. The predicted persistence lengths when applied to the series of three SST nanotubes significantly underestimates the nanotube persistence lengths (Fig. 10). A significant factor in the over-prediction likely lies in the assumption that dsDNA can be considered as a uniform elastic rod. Given the structure of DNA—it has a tightly-packed core of stacked and paired bases and, due to the major and minor grooves, a shape more akin to an asymmetric double-threaded screw than a cylindrical rod—it is perhaps not surprising this may not be the best approximation. If we consider  $r$  to be a parameter, we can find the value that best fits the SST nanotube data; this fitting gives an effective radius of 0.65 nm, with the resulting form capturing well the dependence on  $n_{\text{helix}}$ . This compares to 1.15 nm used in the original prediction, which is a measure of the limits of the excluded volume of an oxDNA double helix.

There is some variation of the persistence lengths for those helix bundles with the same numbers of helices. For example, for the six-helix bundles  $l_b$  varies between 4160 and 7650 nm and  $l_t/2$  between 620 and 810 nm. Although one in principle expects the persistence lengths to also depend somewhat on the types of junction (single or double crossover), the patterns of nicks and junctions, tube radius (Eq. 23) and the degree of internal stress, a significant part of this variation is probably down to errors due to imperfect sampling; as mentioned earlier, the 4HB-MT and 6HB-MT examples suffer particularly in this regard with the tangent-tangent correlations lacking the clear exponential tail that is expected for a worm-like chain. One systematic feature, which seems robust, is that the SST nanotubes have a larger bending persistence. This is perhaps surprising, as one might have expected them to be more flexible given that they have single rather than double crossovers at the junctions. The most likely reason is that the extra freedom associated with the single crossover allows the nucleotides at the junctions to better optimize their stacking interactions, causing the junctions to actually be stiffer.

We can also compare our results to the available experimental data for these systems, which are included where available in Table 1. Although the persistence length of the 10HB origami design considered here has not been determined experimentally, a value of 5430 nm was obtained for a very similar 10HB design.<sup>31</sup> In all cases the oxDNA values for the bending persistence length are larger. One clear factor is that the simulations have been performed for origamis with the ideal structures, whereas there is likely to be imperfections in the experimental origamis due both to assembly errors, be it a result of missing staples or the incorrect routing of the strands, and to errors in the synthesis of the staples. Quantitative evidence has been obtained for the presence of such assembly errors,<sup>78–80</sup> but estimates of their prevalence have varied significantly. For example, Ref. 80 estimated that on average only 84% of staples were incorporated into a 2D origami, whereas Ref. 78 obtained folding qualities of 96% or greater for 3D origamis. The resulting defects could well lead to both local static structural irregularities and enhanced fluctuations, both of which would

contribute to lowering the measured persistence lengths. From this viewpoint, the experimentally measured values should be seen as lower bounds to the persistence lengths of ideal structures.

The substantial effect of defects on the mechanical properties has been confirmed in experiments that deliberately introduce defects into origami structures. For example, gaps between staple ends reduce bend persistence lengths<sup>31</sup> and gaps and nicks reduce the effects of torsional stresses<sup>81,82</sup> (i.e. they reduce the local twist modulus of the origami). Similarly, missing staples have been used to achieve designs with higher local mechanical compliance.<sup>83,84</sup> Radiation damage has also been found to make a 6HB origami more flexible.<sup>85</sup>

Another factor that we should mention is that in our calculations we choose to ignore the ends of the origami due to their enhanced fluctuations, which would otherwise introduce some degree of non-worm-like chain behaviour and a lowering of the persistence lengths. However, these effects are relatively small. Also, our  $m$ -dependent definition of the bending persistence length shows a significant length dependence. However, this is due to enhanced local fluctuations at the shortest length scales, whereas the experimental measurements are unlikely to be sensitive to these effects, both due to the lower resolution of the molecular contour and the analysis methods used. Similarly, these length-dependent effects are dramatically reduced when we use the averaging approach of Section 2.7 (Fig. S13(c))

The most accurate persistence length measurements are probably those of Ref. 32 because the lengths of the SST nanotubes can be significantly larger than an origami. By visualizing the molecular contours of individual tubes as a function of time they were able to measure the tangent-tangent correlation of individual nanotubes over length scales of up to about  $10 \mu\text{m}$ . One interesting feature of the results was that the variation of the persistence lengths between different examples of the same design was greater than the estimated error in the persistence length for an individual tube. So for the 6HB, the persistence lengths varied between  $1.6$  and  $4.7 \mu\text{m}$ , and between  $5.7$  and  $10.1 \mu\text{m}$  for the 8HB. This indicates that the population of nanotubes has a heterogeneous set of mechanical properties. In this case, there is a possible

isomerism (associated with whether the strands are in registry or offset as one goes around the circumference of the tube) that may be partly responsible for this heterogeneity, but it is also likely to reflect differences in the assembly quality of individual nanotubes. For this reason, the highest values may provide the best estimates of the persistence lengths of the ideal nanotubes (the average values are reported in Table 1).

The difference between the experimental and oxDNA values could also reflect deficiencies in the oxDNA model. One known shortcoming is that although oxDNA reproduces well the bend and twist persistence lengths of dsDNA, it considerably overestimates the stretch modulus. For the original oxDNA model the extensional modulus is about 2100 pN,<sup>69</sup> but it has not previously been calculated for the second version of the model used here (sometimes called “oxDNA2”). Fitting the force-extension curve of dsDNA to the extensible worm-like chain form (Fig. S22) gives an estimate of about 2700 pN for oxDNA2. This compares to experimental estimates of about 1200 pN at high salt conditions.<sup>86</sup> The bending of a helix bundle not only involves the bending of the individual helices, but also leads the helices on the inside of the bend to be compressed, and those on the outside to be in tension. Thus, that the oxDNA extensional modulus is too large is likely to contribute to an overestimation of the bending persistence lengths. Note, though, that the tube can also respond to the tension and compression by changing its local structure, e.g. by changing the splay angle of the helices at junctions and hence the interhelix separation.

In Table 1, we report the limiting values of the elastic moduli for all systems. Note that we do not give values for the coupling terms  $A_{12}$ ,  $G_1$  and  $G_2$  as there is no strong evidence that non-zero values are more than statistical noise. For completeness, we plot their  $m$ -dependent values in Figs. S23–S26, but it is noteworthy that rather than rising smoothly to their limiting values—as is the case for  $A_1$ ,  $A_2$  and  $C$ , as well as the twist-bend coupling constant for dsDNA<sup>56</sup>—they are generally close to zero for small values of  $m$ , where the statistics are best, with any significant deviations from zero occurring at larger  $m$ . However, as we estimate the limiting values of  $A_1$ ,  $A_2$  and  $C$  from the large- $m$  behaviour, the non-zero

values of the off-diagonal terms are likely to somewhat affect the accuracy of these elastic moduli.

It was expected based on approximate symmetry that for all systems, except for 4HB-SST and the 10HB origami,  $A_1$  and  $A_2$  would be approximately equal. This is generally the case with differences being at most 25%. For the 6HB and 8HB SST nanotubes for which there is an exact symmetry due to the regularity of their junctions,  $A_1$  and  $A_2$  are virtually exactly equal.

The large difference in  $A_1$  and  $A_2$  for the 10HB is expected given its very anisotropic cross-section. The origin of this difference for the 4HB-SST system is more subtle. As a consequence of the alternating pattern of 10 and 11 base-pair spacings between junctions in the SST nanotubes, the interhelix angles alternate on going around the nanotube. This leads to the diamond, rather than square, tube cross-section apparent in Fig. 2(a). This effect can be quantified by measuring the distance of equivalent helices in the SST nanotubes from the tube centre. These two distances are shown in Fig. 9(b) for the 4HB-SST and in Fig. S28 for the other SST tubes. The difference in the two distances is roughly 0.4–0.5 nm for the 4HB-SST tube.

If  $A_{12} = G_1 = G_2 = 0$  then the bending persistence length should simply be the harmonic mean of the bend elastic constants  $A_1$  and  $A_2$ . This generally holds to within 10%, the exceptions being the MT systems for which the sampling issues affecting the values of  $l_b$  have already been noted. Similarly, if the coupling terms are zero then  $l_t/2 = C$ ; this generally holds to within less than 10%, the exceptions being 4HB-SST and 10HB, for which the large differences between  $A_1$  and  $A_2$  make the obtained limiting value of  $C$  more sensitive to the behaviour of the coupling terms. For the two experimental systems for which the twist modulus has been measured, the oxDNA values are in reasonable agreement, being a bit smaller for the 4HB-MT origami and somewhat larger for the 6HB-MT origami, which happens to have the largest  $C$  of the 6HB systems that we have studied.



## 4 Conclusions

In this paper we have introduced approaches to compute persistence lengths and elastic moduli associated with bending and twisting for rod-like DNA nanostructures. One feature is that only on length scales beyond those associated with the spacings between the junctions do the bending fluctuations behave like those of a worm-like chain. As our discretization was performed at the level of single base-pair steps along the molecular contour, averaging methods had to be introduced to extract bulk values of the elastic moduli. The approaches, although computationally intensive due to the long simulations required to adequately sample the long length-scale fluctuations, are straightforwardly applicable to other DNA nanostructures. Thus, they could be used as part of a rational design process to produce DNA nanostructures with tailored mechanical properties.

In line with previous experiments,<sup>29,31,32</sup> we found that the persistence lengths and elastic moduli associated with bending exhibit a strong non-linear dependence on the number of helices, whereas the twist persistence lengths increase approximately linearly. Consequently, the DNA nanotubes are in a very different mechanical regime with respect to angular deformations compared to duplex DNA. For example, for the six-helix bundles the persistence length is on average about eight times larger than the twist modulus, whereas for dsDNA the twist modulus is over twice as large.

In all cases, the values for the bending persistence lengths that we obtain are larger than those measured experimentally. The main reasons for these differences are firstly that our calculations are performed for ideal structures, whereas the structures in experiments will inevitably have some degree of defects due to both assembly and strand synthesis. Secondly, one of the known deficiencies of the oxDNA model is that it overestimates the stretch modulus of dsDNA, which in turn is likely to lead to the cost of nanotube bending being overestimated as the individual helices will be somewhat compressed on the inside of a bend and stretched on the outside. Note that there are also uncertainties in the accuracy of oxDNA's description of the mechanical properties of junctions and nicks, as there is relatively

little experimental information to which to compare. The relative contributions of these two main factors is not fully clear. However, it is interesting to note that oxDNA is able to reproduce well the bending and twisting of the example origamis in Ref. 20 that result from internal stresses induced by insertions and deletions, and that partly reflect the elastic moduli of the origami.<sup>54</sup>

Here, we have characterized the elastic fluctuations of a set of DNA nanostructures. It would also be of interest to go beyond the elastic regime to explore their response to external stresses, in particular how they buckle under extreme twist and bending. Their generic behaviour could well be quite different from dsDNA, because of the very different ratios of the bend to twist moduli. For example, would they form plectonemes in the same way that dsDNA does under extreme twists, or would the costs of bending the nanotube back on itself at the tip of the plectoneme be prohibitive?

## Acknowledgement

We thank Magdalen College, Oxford for the award of a Perkin Research Scholarship (HC), and are grateful for support from the EPSRC Centre for Doctoral Training, Theory and Modelling in Chemical Sciences, under grant EP/L015722/1 (HC and DP), from the Department of Science and Technology India under grant DST/INSPIRE/04/2014/002085 (GM), from the European Union’s Horizon 2020 research and innovation programme under Marie Skłodowska-Curie Grant Agreement No. 641839 (MMCT), and from “Fonds voor Wetenschappelijk Onderzoek” under project number 1SB4219N (ES). We acknowledge the use of computational facilities provided by the University of Oxford Advanced Research Computing [doi:10.5281/zenodo.22558] and Calcul Quebec.

## Supporting Information Available

The following files are available free of charge.

The Supporting Information is available free of charge on the ACS Publications website at DOI: 10.1021/acs.jctc.XXXX

- Additional details on the simulations and their equilibration; triad vector definitions; further snapshots of the nanostructures; further results both to support the methodological developments and to provide a fuller characterization of the structure and mechanical properties of all systems.

## References

- (1) Rothmund, P. W. K. Folding DNA to create nanoscale shapes and patterns. *Nature* **2006**, *440*, 297–302.
- (2) Yin, P.; Hariadi, R. F.; Sahu, S.; Choi, H. M. T.; Park, S. H.; LaBean, T. H.; Reif, J. H. Programming DNA tube circumferences. *Science* **2008**, *321*, 824–826.
- (3) Wei, B.; Dai, M.; Yin, P. Complex shapes self-assembled from single-stranded DNA tiles. *Nature* **2012**, *485*, 623–626.
- (4) Ke, Y.; Ong, L. L.; Shih, W. M.; Yin, P. Three-dimensional structures self-assembled from DNA bricks. *Science* **2012**, *338*, 1177–1183.
- (5) Hong, F.; Zhang, F.; Liu, Y.; Yan, H. DNA origami: Scaffolds for creating higher order structures. *Chem. Rev.* **2017**, *117*, 12584–12640.
- (6) Ramezani, H.; Dietz, H. Building machines with DNA molecules. *Nat. Rev. Genet.* **2020**, *21*, 5–26.
- (7) Pfeifer, W.; Sacca, B. Synthetic DNA filaments: from designs to applications. *Biol. Chem.* **2018**, *399*, 773–785.
- (8) Bai, X.-C.; Martin, T. G.; Scheres, S. H. W.; Dietz, H. Cryo-EM structure of a 3D DNA-origami object. *Proc. Natl. Acad. Sci. USA* **2012**, *109*, 20012–20017.

- (9) Blanchard, A. T.; Salaita, K. Emerging uses of DNA mechanical devices. *Science* **2019**, *365*, 1080–1081.
- (10) Gosse, C.; Strick, T. R.; Kostrz, D. Molecular scaffolds: when DNA becomes the hardware for single-molecule investigations. *Curr. Opin. Chem. Biol.* **2019**, *53*, 192–203.
- (11) Pfitzner, E.; Wachauf, C.; Kilchherr, F.; Pelz, B.; Shih, W. M.; Rief, M.; Dietz, H. Rigid DNA beams for high-resolution single-molecule mechanics. *Angew. Chem. Int. Ed.* **2013**, *52*, 7766–7771.
- (12) Kilchherr, F.; Wachauf, C.; Pelz, B.; Rief, M.; Zacharias, H., M. Dietz Single-molecule dissection of stacking forces in DNA. *Angew. Chem. Int. Ed.* **2016**, *353*, aaf5508.
- (13) Dutta, P. K.; Zhang, Y.; Blanchard, A. T.; Ge, C.; Rushdi, M.; Weiss, K.; Zhu, C.; Ke, Y.; Salaita, K. Programmable multi-valent DNA-origami tension probes for reporting cellular traction forces. *Nano Lett.* **2018**, *18*, 4803–4811.
- (14) Funke, J. J.; Ketterer, P.; Lieleg, C.; Korber, P.; Dietz, H. Exploring nucleosome unwrapping using DNA origami. *Nano Lett.* **2016**, *16*, 7891–7898.
- (15) Le, J. V.; Luo, Y.; Darcy, M. A.; Lucas, C. R.; Goodwin, M. F.; Poirier, M. G.; Castro, C. E. Probing nucleosome stability with a DNA origami nanocaliper. *ACS Nano* **2016**, *10*, 7073–7084.
- (16) Nickels, P. C.; Wünsch, B.; Holzmeister, P.; Bae, W.; Kneer, L. M.; Grohmann, D.; Tinnefeld, P.; Liedl, T. Molecular force spectroscopy with a DNA origami-based nanoscopic force clamp. *Science* **2016**, *354*, 305–307.
- (17) Kramm, K.; Schröder, T.; Gouge, J.; Vera, A. M.; Heiss, F. B.; Liedl, T.; Engel, C.; Berger, I.; Vannini, A.; Tinnefeld, P.; Grohmann, D. DNA origami-based single-molecule force spectroscopy elucidates RNA Polymerase III pre-initiation complex stability. *Nat. Commun.* **2020**, *11*, 2828.

- (18) Funke, J. J.; Ketterer, P.; Lieleg, C.; Schunter, S.; Korber, P.; Dietz, H. Uncovering the forces between nucleosomes using DNA origami. *Sci. Adv.* **2016**, *2*, e1600974.
- (19) Ke, Y.; Meyer, T.; Shih, W. M.; Bellot, G. Regulation at a distance of biomolecular interactions using a DNA nanoactuator. *Nat. Commun.* **2016**, *7*, 10935.
- (20) Dietz, H.; Douglas, S. M.; Shih, W. M. Folding DNA into twisted and curved nanoscale shapes. *Science* **2009**, *325*, 725–730.
- (21) Liedl, T.; Högberg, B.; Tytell, J.; Ingber, D. E.; Shih, W. M. Self-assembly of three-dimensional prestressed tensegrity structures from DNA. *Nat. Nanotechnol.* **2010**, *5*, 520–524.
- (22) Zhou, L.; Marras, A. E.; Castro, C. E. Origami Compliant Nanostructures with Tunable Mechanical Properties. *ACS Nano* **2014**, *8*, 27–34.
- (23) Suzuki, Y.; Kawamata, I.; Mizuno, K.; Murata, S. Large deformation of a DNA origami nanoarm through the cumulative actuation of tension-adjustable modules. *Angew. Chem. Int. Ed.* **2020**, *59*, 6230–6234.
- (24) Zhou, L.; Marras, A. E.; Su, H.-J.; Castro, C. E. Direct design of an energy landscape with bistable DNA origami mechanisms. *Nano Lett.* **2015**, *15*, 1815–1821.
- (25) Bustamante, C.; Bryant, Z.; Smith, S. B. Ten years of tension: single-molecule DNA mechanics. *Nature* **2003**, *421*, 423–427.
- (26) Brahmachari, S.; Marko, J. F. In *Biomechanics in Oncology*; Dong, C., Zahir, N., Konstantopoulos, K., Eds.; Adv. Exp. Med. Biol.; Springer, 2018; Vol. 1092; pp 11–39.
- (27) Romano, F.; Chakraborty, D.; Doye, J. P. K.; Ouldridge, T. E.; Louis, A. A. Coarse-grained simulations of DNA overstretching. *J. Chem. Phys.* **2013**, *138*, 085101.

- (28) Marin-Gonzalez, A.; Vilhena, J. G.; Perez, R.; Moreno, F. Understanding the mechanical response of double-stranded DNA and RNA under constant stretching forces using all-atom molecular dynamics. *Proc. Natl. Acad. Sci. USA* **2017**, *114*, 7049–7054.
- (29) Kauert, D. J.; Kurth, T.; Liedl, T.; Seidel, R. Direct mechanical measurements reveal the material properties of three-dimensional DNA origami. *Nano Lett.* **2011**, *11*, 5558–5563.
- (30) Castro, C. E.; Su, H.-J.; Marras, A. E.; Zhou, L.; Johnson, J. Mechanical design of DNA nanostructures. *Nanoscale* **2015**, *7*, 5913–5921.
- (31) Lee, C.; Kim, K. S.; Kim, Y.-J.; Lee, J. Y.; Kim, D.-N. Tailoring the Mechanical Stiffness of DNA Nanostructures Using Engineered Defects. *ACS Nano* **2019**, *13*, 8329–8336.
- (32) Schiffels, D.; Liedl, T.; Fygenson, D. K. Nanoscale structure and microscale stiffness of DNA nanotubes. *ACS Nano* **2013**, *7*, 6700–6710.
- (33) Rothmund, P. W. K.; Ekani-Nkodo, A.; Papadakis, N.; Kumar, A.; Fygenson, D. K.; Winfree, E. Design and characterization of programmable DNA nanotubes. *J. Am. Chem. Soc.* **2004**, *126*, 16344–16353.
- (34) O’Neill, P.; Rothmund, P. W. K.; Kumar, A.; Fygenson, D. K. Sturdier DNA nanotubes via ligation. *Nano Lett.* **2006**, *6*, 1379–1383.
- (35) Wang, T.; Schiffels, D.; Martinez Cuesta, S.; Fygenson, D. K. Design and characterization of 1D nanotubes and 2D periodic arrays self-assembled from DNA multi-helix bundles. *J. Am. Chem. Soc.* **2012**, *134*, 1606–1616.
- (36) Benson, E.; Mohammed, A.; Rayneau-Kirkhope, D.; Gøadin, A.; Orponen, P.; Högborg, B. Effects of design choices on the stiffness of wireframe DNA origami structures. *ACS Nano* **2018**, *12*, 9291–9299.

- (37) Benson, E.; Lolaico, M.; Tarasov, Y.; Gøadin, A.; Högberg, B. Evolutionary refinement of DNA nanostructures using coarse-grained molecular dynamics simulations. *ACS Nano* **2019**, *13*, 12591–12598.
- (38) Pfeifer, W.; Lill, P.; Gatsogiannis, C.; Sacca, B. Hierarchical assembly of DNA filaments with designer elastic properties. *ACS Nano* **2018**, *12*, 44–55.
- (39) Ma, Z.; Kawai, K.; ; Hirai, Y.; Tsuchiva, T.; Tabata, O. Tuning porosity and radial mechanical properties of DNA origami nanotubes via crossover design. *Jpn. J. Appl. Phys.* **2017**, *56*, 06GJ02.
- (40) Bae, W.; Kim, K.; Min, D.; Ryu, J.-K.; Hyeon, C.; Yoon, T.-Y. Programmed folding of DNA origami structures through single-molecule force control. *Nat. Commun.* **2014**, *5*, 5654.
- (41) Koirala, D.; Shrestha, P.; Emura, T.; Hidaka, K.; Mandal, S.; Endo, M.; Sugiyama, H.; Mao, H. Single-molecule mechanochemical sensing using DNA origami nanostructures. *Angew. Chem. Int. Ed.* **2014**, *53*, 8137–8141.
- (42) Shrestha, P.; Emura, T.; Koirala, D.; Cui, Y.; Hidaka, K.; Maximuck, W. J.; Endo, M.; Sugiyama, H.; Mao, H. Mechanical properties of DNA origami nanoassemblies are determined by Holliday junction mechanophores. *Nucleic Acids Res.* **2016**, *44*, 6574–6582.
- (43) Engel, M. C.; Smith, D. M.; Jobst, M. A.; Sajfutdinow, M.; Liedl, T.; Romano, F.; Rovigatti, L.; Louis, A. A.; Doye, J. P. K. Force-induced unravelling of DNA origami. *ACS Nano* **2018**, *12*, 6734–6747.
- (44) Yoo, J.; Aksimentiev, A. In situ structure and dynamics of DNA origami determined through molecular dynamics simulations. *Proc. Natl. Acad. Sci. USA* **2013**, *110*, 20099–20104.

- (45) Göpfrich, K.; Li, C.-Y.; Ricci, M.; Bhamidimarri, S. P.; Yoo, J.; Gyenes, B.; Ohmann, A.; Winterhalter, M.; Aksimentiev, A.; Keyser, U. F. Large-conductance transmembrane porin made from DNA origami. *ACS Nano* **2016**, *10*, 8207–8214.
- (46) Sloane, S. M.; Li, C.-Y.; Yoo, J.; Aksimentiev, A. Molecular mechanics of DNA bricks: in situ structure, mechanical properties and ionic conductivity. *New J. Phys.* **2016**, *18*, 055012.
- (47) Joshi, H.; Dwaraknath, A.; Maiti, P. K. Structure, stability and elasticity of DNA nanotubes. *Phys. Chem. Chem. Phys.* **2015**, *17*, 1424–1434.
- (48) Joshi, H.; Kaushnik, A.; Seeman, N. C.; Maiti, P. K. Nanoscale structure and elasticity of pillared DNA nanotubes. *ACS Nano* **2016**, *10*, 7780–7791.
- (49) Naskar, S.; Gosika, M.; Joshi, H.; Maiti, P. K. Tuning the stability of DNA nanotubes with salt. *J. Phys. Chem. C* **2019**, *123*, 9461–9470.
- (50) Castro, C. E.; Kilchherr, F.; Kim, D.-N.; Shiao, E. L.; Wauer, T.; Wortmann, P.; Bathe, M.; Dietz, H. A primer to scaffolded DNA origami. *Nat. Methods* **2011**, *8*, 221–229.
- (51) Kim, D.-N.; Kilchherr, F.; Dietz, H.; Bathe, M. Quantitative prediction of 3D solution shape flexibility of nucleic acid nanostructures. *Nucleic Acids Res.* **2012**, *40*, 2862–2868.
- (52) Maffeo, C.; Aksimentiev, A. MrDNA: A multi-resolution model for predicting the structure and dynamics of DNA systems. *Nucleic Acids Res.* **2020**, *48*, 5135–5146.
- (53) Kim, Y.-J.; Kim, D.-N. Sensitivity analysis for the mechanical properties of DNA bundles. *J. Nanomater.* **2016**, *11*, 6287937.
- (54) Snodin, B. E. K.; Randisi, F.; Mosayebi, M.; Šulc, P.; Schreck, J. S.; Romano, F.; Ouldrige, T. E.; Tsukanov, R.; Nir, E.; Louis, A. A.; Doye, J. P. K. Introducing



- improved structural properties and salt dependence into a coarse-grained model of DNA. *J. Chem. Phys.* **2015**, *142*, 234901.
- (55) Nomidis, S. K.; Kriegel, F.; Vanderlinden, W.; Lipfert, J.; Carlon, E. Twist-bend coupling and the torsional response of double-stranded DNA. *Phys. Rev. Lett.* **2017**, *118*, 217801.
- (56) Skoruppa, E.; Laleman, M.; Nomidis, S. K.; Carlon, E. DNA elasticity from coarse-grained simulations: The effect of groove asymmetry. *J. Chem. Phys.* **2017**, *146*, 214902.
- (57) Matek, C.; Ouldridge, T. E.; Doye, J. P. K.; Louis, A. A. Plectoneme tip bubbles: Coupled denaturation and writhing in supercoiled DNA. *Sci. Rep.* **2015**, *5*, 7655.
- (58) Sharma, R.; Schreck, J. S.; Romano, F.; Louis, A. A.; Doye, J. P. K. Characterizing the motion of jointed DNA nanostructures using a coarse-grained model. *ACS Nano* **2017**, *11*, 12426–12435.
- (59) Shi, Z.; Castro, C. E.; Arya, G. Conformational dynamics of mechanically compliant DNA nanostructures from coarse-grained molecular dynamics simulations. *ACS Nano* **2017**, *11*, 4617–4630.
- (60) Zhou, L.; Marras, A. E.; Huang, C.-M.; Castro, C. E.; Su, H.-J. Paper origami-inspired design and actuation of DNA nanomachines with complex motions. *Small* **2018**, *14*, 1802580.
- (61) Snodin, B. E. K.; Schreck, J. S.; Romano, F.; Louis, A. A.; Doye, J. P. K. Coarse-grained modelling of the structural properties of DNA origami. *Nucleic Acids Res.* **2019**, *47*, 1585–1597.
- (62) Berengut, J. F.; Berengut, J. C.; Doye, J. P. K.; Prešern, D.; Kawanoto, A.; Ruan, J.;

- Wainwright, M. J.; Lee, L. K. Design and synthesis of pleated DNA origami nanotubes with adjustable diameters. *Nucleic Acids Res.* **2019**, *47*, 11963–11975.
- (63) Suma, A.; Stopar, A.; Nicholson, A. W.; Castronovo, M.; Carnevale, V. Global and local mechanical properties control endonuclease reactivity of a DNA origami nanostructure. *Nucleic Acids Res.* **2020**, *48*, 4672–4689.
- (64) Schreck, J. S.; Romano, F.; Zimmer, M. H.; Louis, A. A.; Doye, J. P. K. Characterizing DNA star-tile-based nanostructures using a coarse-grained model. *ACS Nano* **2016**, *10*, 4236–4247.
- (65) Hong, F.; Jiang, S.; Lan, X.; Narayanan, R. P.; Šulc, P.; Zhang, F.; Liu, Y.; Yan, H. Layered-crossover tiles with precisely tunable angles for 2D and 3D DNA crystal engineering. *J. Am. Chem. Soc.* **2018**, *140*, 14670–14676.
- (66) Matthies, M.; Agarwal, N. P.; Poppleton, E.; Joshi, F. M.; Šulc, P.; Schmidt, T. L. Triangulated wireframe structures assembled using single-stranded DNA tiles. *ACS Nano* **2019**, *13*.
- (67) Tortora, M. M. C.; Mishra, G.; Prešern, D.; Doye, J. P. K. Chiral shape fluctuations and the origin of chirality in cholesteric phases of DNA origamis. *Sci. Adv.* **2020**, *6*, accepted.
- (68) Siavashpouri, M.; Wachauf, C. H.; Zakhary, M. J.; Praetorius, F.; Dietz, H.; Dogic, Z. Molecular engineering of chiral colloidal liquid crystals using DNA origami. *Nat. Mater.* **2017**, *16*, 849–856.
- (69) Ouldridge, T. E.; Louis, A. A.; Doye, J. P. K. Structural, mechanical and thermodynamic properties of a coarse-grained DNA model. *J. Chem. Phys.* **2011**, *134*, 085101.
- (70) Šulc, P.; Romano, F.; Ouldridge, T. E.; Rovigatti, L.; Doye, J. P. K.; Louis, A. A. In-

- roducing sequence-dependent interactions into a coarse-grained DNA model. *J. Chem. Phys.* **2012**, *137*, 135101.
- (71) Russo, J.; Tartaglia, P.; Sciortino, F. Reversible gels of patchy particles: Role of the valence. *J. Chem. Phys.* **2009**, *131*, 014504.
- (72) Marko, J. F.; Siggia, E. D. Bending and twisting elasticity of DNA. *Macromolecules* **1994**, *27*, 981–988.
- (73) Skoruppa, E. DNA elasticity from coarse-grained simulations: On the hunt for twist-bend coupling. M.Sc. thesis, KU Leuven, 2017.
- (74) Wiggins, P. A.; Nelson, P. C. Generalized theory of semiflexible polymers. *Phys. Rev. E* **2006**, *73*, 031906.
- (75) Nomidis, S. K.; Skoruppa, E.; Carlon, E.; Marko, J. F. Twist-bend coupling and the statistical mechanics of DNA: Perturbation theory and beyond. *Phys. Rev. E* **2019**, *99*, 032414.
- (76) Strang, G. *Linear Algebra and Its Applications*; Brooks Cole, 2006.
- (77) Baker, M. A. B.; Tuckwell, A. J.; Berengut, J. F.; Bath, J.; Benn, F.; Duff, A. P.; Whitten, A. E.; Dunn, K. E.; Hynson, R. M.; Turberfield, A. J.; Lee, L. K. Dimensions and global twist of single-layer DNA origami measured by small-angle X-ray scattering. *ACS Nano* **2018**, *12*, 5791–5799.
- (78) Wagenbauer, K. F.; Wachauf, C. H.; Dietz, H. Quantifying quality in DNA self-assembly. *Nat. Commun.* **2014**, *5*, 3691.
- (79) Muschol, C.; Baym, M.; Hanikel, N.; Ong, L. L.; Gootenberg, J. S.; Yin, P. Barcode extension for analysis and reconstruction of structures. *Nat. Commun.* **2017**, *8*, 14698.

- (80) Straus, M. T.; Scheuder, F.; Haas, D.; Nickels, P. C.; Jungmann, R. Quantifying absolute addressability in DNA origami with molecular resolution. *Nat. Commun.* **2018**, *9*, 1600.
- (81) Kim, Y.-J.; Lee, C.; Lee, J. G.; Kim, D.-N. Configurational design of mechanical perturbation for fine control of twisted DNA origami structures. *ACS Nano* **2019**, *13*, 6348–6355.
- (82) Lee, J. Y.; Kim, Y.-J.; Lee, C.; Lee, J. G.; Yagyu, H.; Tabata, O.; Kim, D.-N. Investigating the sequence-dependent mechanical properties of DNA nicks for applications in twisted DNA nanostructure design. *Nucleic Acids Res.* **2019**, *47*, 93–102.
- (83) Lee, C.; Lee, J. Y.; Kim, D.-N. Polymorphic design of DNA origami structures through mechanical control of modular components. *Nat. Commun.* **2017**, *8*, 2067.
- (84) Turek, V. A.; Chikkaraddy, R.; Cormier, S.; Stockhahm, B.; Ding, T.; Keyser, U. F. Thermo-Responsive Actuation of a DNA Origami Flexor. *Adv. Funct. Mater.* **2018**, *28*, 1706410.
- (85) Fang, W.; Xie, M.; Hou, X.; Liu, X.; Zuo, X.; Chao, J.; Wang, L.; Fan, C.; Liu, H.; Wang, L. DNA origami radiometers for measuring ultraviolet exposure. *J. Am. Chem. Soc.* **2020**,
- (86) Wang, M. D.; Yin, H.; Landick, R.; Geiles, J.; Block, S. M. Stretching DNA with optical tweezers. *Biophys. J.* **1997**, *72*, 1335–1346.

# Supporting Information

## S1 Further simulation snapshots

Simulation snapshots of some of the systems not visualized in the main text are given in Figures S1, S2 and S3. (Some snapshots of the twisted origami nanotubes can be found in Ref. 67.) The snapshots give an impression of the scale of typical bending fluctuations. Apparent from the end views of 6HB-SST and 8HB-SST is the departure of their cross-sections from a regular hexagonal and octagonal form, respectively, due to the alternating inter-helix angles in these systems, an effect noted for 4HB-SST in the main text.

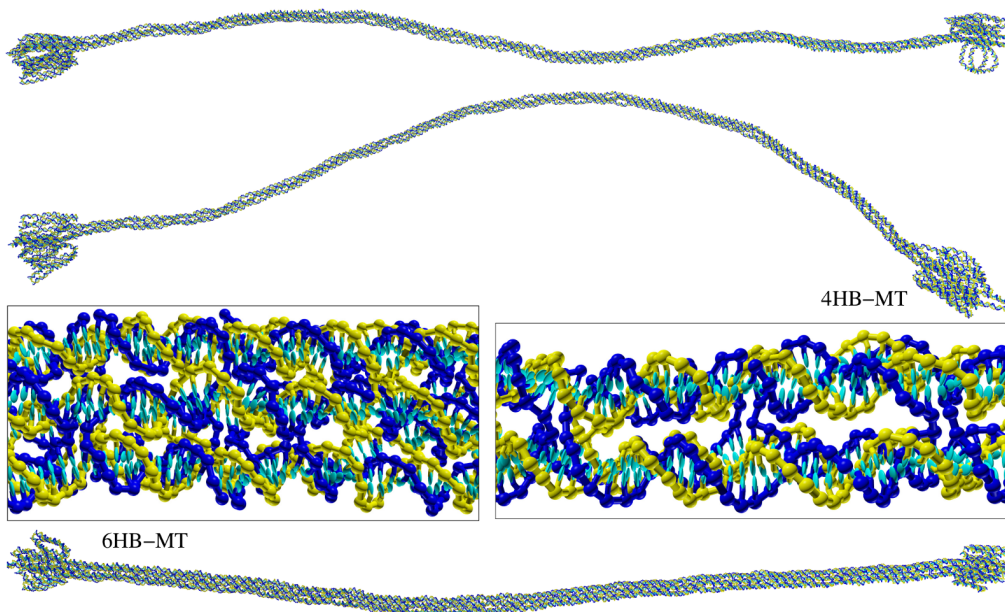


Figure S1: Snapshots of the 4HB-MT and 6HB-MT origami. The second image of the 4HB-MT origami shows an exceptionally bent configuration. The blocks at each end of the origamis are to facilitate attachment to the beads in magnetic tweezer experiments.

## S2 Further Equilibration and Simulation details

Figure S4 shows the end-to-end distance in the molecular dynamics trajectories for four example systems. The 6HB-SST nanotube shows relatively fast fluctuations over the range

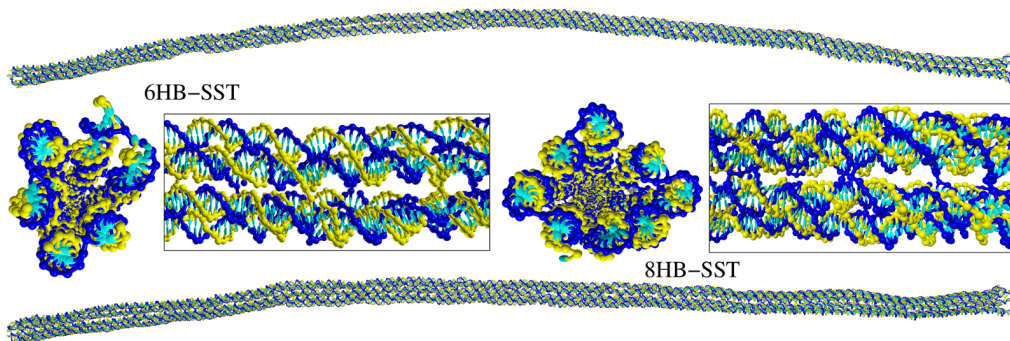


Figure S2: Snapshots of the 6HB-SST and 8HB-SST nanotubes. The end views clearly show the alternating distances of the helices from the centres of the tubes.

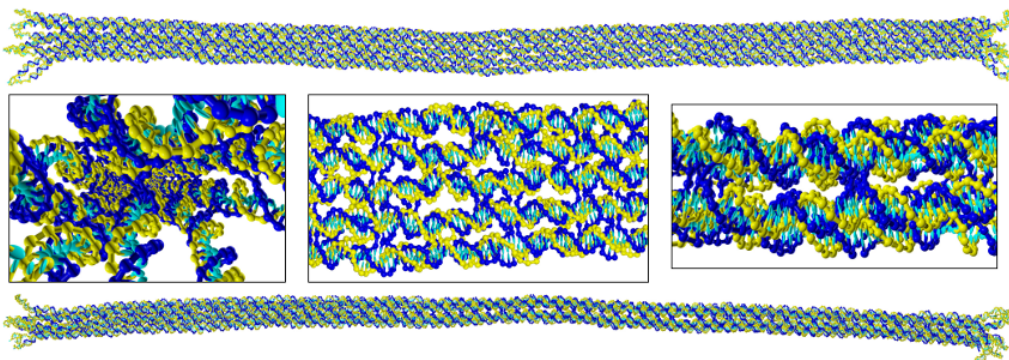


Figure S3: Snapshots of the 10HB origami. The two side views are roughly perpendicular to their thick and thin dimensions. Note this is not perfectly maintained because of the slight right-handed twist of the origami.

of end-to-end distances it samples. An origami system with the same number of helices (6HB-S) exhibits both a wider range of end-to-end distances (reflecting its lower bend persistence length) and a slower sampling of those distances. In the main text we have suggested the latter may be due to the more constrained nature of the junctions in origamis and a coupling of bending to changes in junction geometry. It is noticeable that distributions of  $\Omega_1$  and  $\Omega_2$  for the origamis have a greater degree of non-Gaussianity than for the SST nanotubes (Figs. S5-S7). Another possible source of slow dynamics is if there is a coupling of more extreme bending with base-pair breaking (note that all the 6HB origamis have some very short 2 base-pair binding domains).

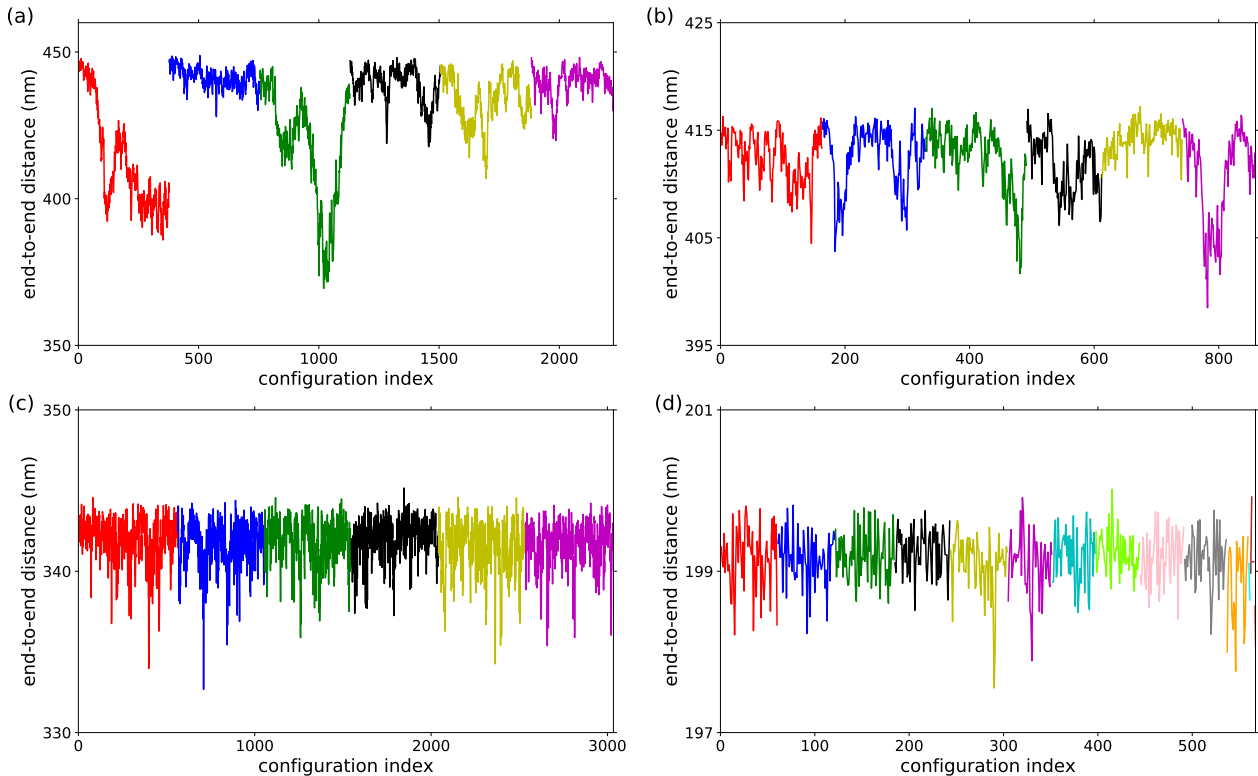


Figure S4: The fluctuation of the “end-to-end” distance during the molecular dynamics trajectories for (a) 4HB-MT, (b) 6HB-S, (c) 6HB-SST and (d) 10HB. The different colours represent separate trajectories. Each configuration is separated by  $6.06 \mu\text{s}$ . In order for the measure to capture the fluctuations of the molecular contour in the bulk of the tube, the distance is measured between slices that are 100 slices in from each end.

The plot for the 4HB-MT shows even slower dynamics and parts of the trajectory show fluctuation to anomalously bent configurations. The former may be partly due to the effects

Table S1: Details of the simulations and the parameters used when calculating elastic properties.  $t_{\text{sim}}$  is the total simulation time of the trajectories.  $N_{\text{config}}$  is the number of configurations in the ensemble used to calculate the elastic properties of each system.  $N_{\text{ends}}$  is the number of slices at each end that are ignored in these calculations.  $2n_{\text{avg}}^X + 1$  is the number of slices over which averaging is performed in Eq. (21) for the elastic constant  $X$ .  $m_{\text{limit}}$  is the value of  $m$  used when taking the limiting values of the elastic constants.

	$t_{\text{sim}}/\text{ms}$	$N_{\text{config}}$	$N_{\text{ends}}$	$n_{\text{avg}}^{A_1}$	$n_{\text{avg}}^{A_2}$	$n_{\text{avg}}^C$	$m_{\text{limit}}$
4HB-MT	13.48	2225	60	20	20	5	600
4HB-SST	6.81	1124	60	15	15	5	600
6HB-2×LH	8.52	1406	60	20	20	5	600
6HB-1×LH	8.05	1328	60	20	20	5	600
6HB-S	5.21	859	60	20	20	5	600
6HB-1×RH	8.34	1376	60	20	20	5	600
6HB-MT	13.33	2199	60	20	20	5	600
6HB-SST	18.38	3034	60	20	20	5	600
8HB-SST	13.91	2295	60	40	40	5	600
10HB	3.44	567	60	40	20	5	400

of the blocks on the ends of these origamis, but the reason for the extremely bent configurations (e.g. the second configuration in Fig. S2) is less clear (one unique feature of the 4HB-MT design is that it has some junctions where one helix has a nick on the strand not involved in the crossover). As a result of this, the statistics for this system are probably the worst. Furthermore, the extreme bending leads to a breakdown of worm-like chain behaviour. For example, the tangent-tangent correlation function lacks a perfectly exponential tail, and that the  $m$ -dependent persistence length exhibits a broad maximum (Fig. S18(a)), rather than smoothly increasing to its limiting value, is a sign that the fluctuations on the longest length scales are greater than one would expect from the (better sampled) shorter length scale fluctuations. That the 6HB-MT origami also exhibits a similar broad maximum (Fig. S18(a)), in contrast to all the other systems, perhaps suggests that this may not simply be a case of insufficient sampling, but that the “MT” origami are behaving somewhat differently. The obvious difference from the other origamis is the blocks on the end, but it is hard to see why these might facilitate anomalously large bending fluctuations on long length scales.



We also include data for the 10HB origami in Fig. S4. This illustrates that as the origami become stiffer the fluctuations become faster and easier to sample.

From the above it is clear that the fluctuations of the SST nanotubes are the most well sampled, and hence the ensembles of configurations are least correlated. It is also noticeable that these systems also have values for the coupling terms that are closest to zero, and in the cases where expected (6HB-SST and 8HB-SST)  $A_1$  and  $A_2$  values that are most similar (Fig. S24). The greater regularity of their pattern of junctions also likely plays a role.

The total simulation time used to generate the configurations and the consequent size of the configurational ensembles used for each system are given in Table S1. It also contains details of the parameters used in our calculations of the mechanical properties.

## S3 Further details of mechanical properties calculations

### S3.1 Angular deformations distributions

The cumulative angular deformations used in Eq. 7 are defined by

$$\Omega_{i,\text{cum}}^{(k)}(m) = \sum_{k=n}^{n+m-1} \Omega_i^{(k)} \quad (\text{S1})$$

The probability distributions of  $a\Omega_{i,\text{cum}}(m)/\sqrt{m}$  for the 4HB-MT and 6HB-MT origamis and the 6HB-SST nanotube for are plotted in Figs. S5–S7, respectively. As expected from the central-limit theorem, the distributions become more Gaussian-like as  $n_{\text{avg}}$  increases, confirming that worm-like chain behaviour holds at longer renormalized length scales. The distributions for the bending deformations become narrower as  $m$  increase, consistent with the increase in the  $m$ -dependent bending elastic constants with  $m$ .

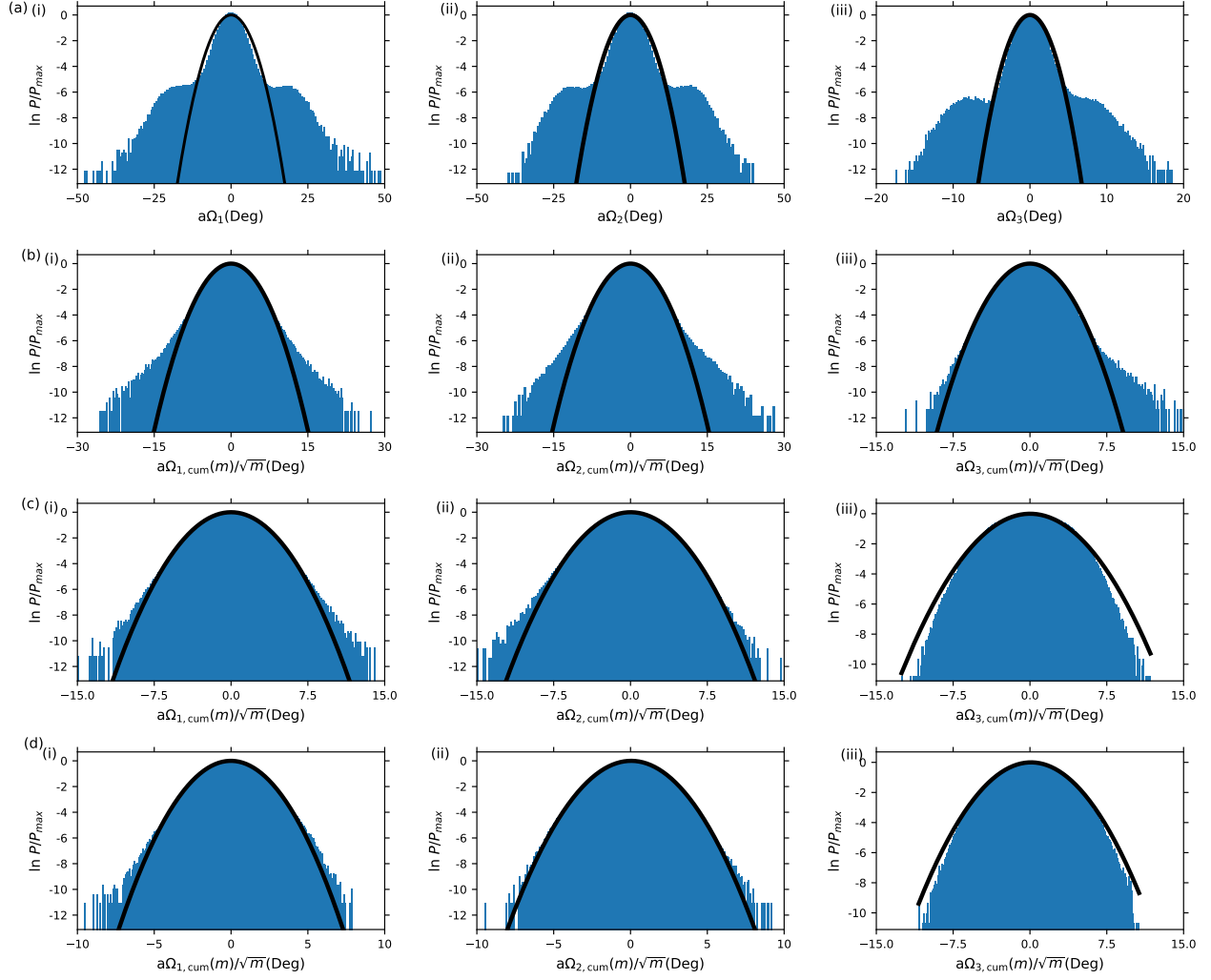


Figure S5: Probability distributions for (i)  $a\Omega_{1,\text{cum}}(m)/\sqrt{m}$ , (ii)  $a\Omega_{2,\text{cum}}(m)/\sqrt{m}$ , and (iii)  $a\Omega_{3,\text{cum}}(m)/\sqrt{m}$  for the 4HB-MT origami at different values of  $m$ : (a)  $m = 1$ , (b)  $m = 3$ , (c)  $m = 11$  and (d)  $m = 41$ . The solid lines are Gaussian fits to the distributions.

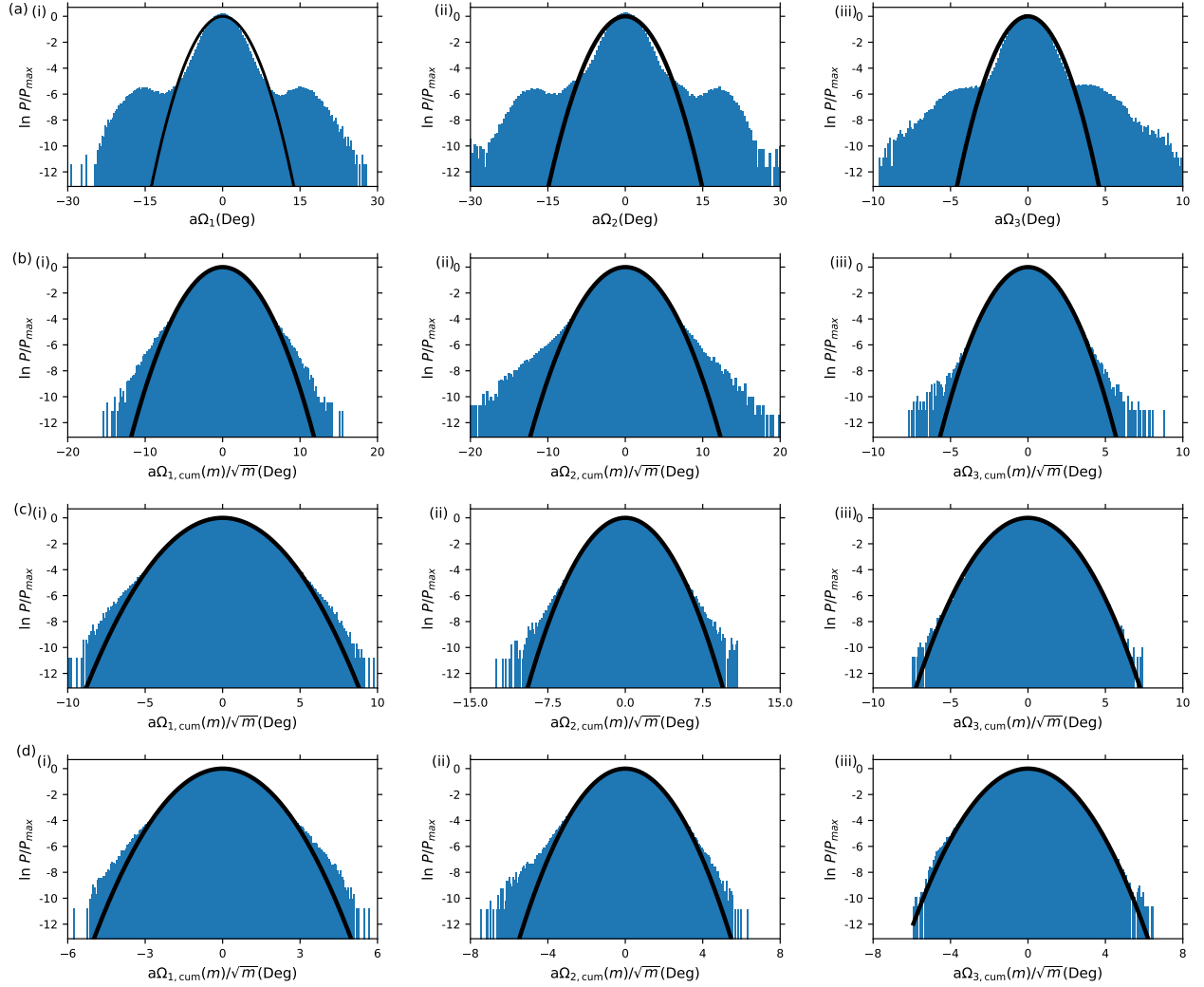


Figure S6: Probability distributions for (i)  $a\Omega_{1,\text{cum}}(m)/\sqrt{m}$ , (ii)  $a\Omega_{2,\text{cum}}(m)/\sqrt{m}$ , and (iii)  $a\Omega_{3,\text{cum}}(m)/\sqrt{m}$  for the 6HB-MT origami at different values of  $m$ : (a)  $m = 1$ , (b)  $m = 3$ , (c)  $m = 11$  and (d)  $m = 41$ . The solid lines are Gaussian fits to the distributions.

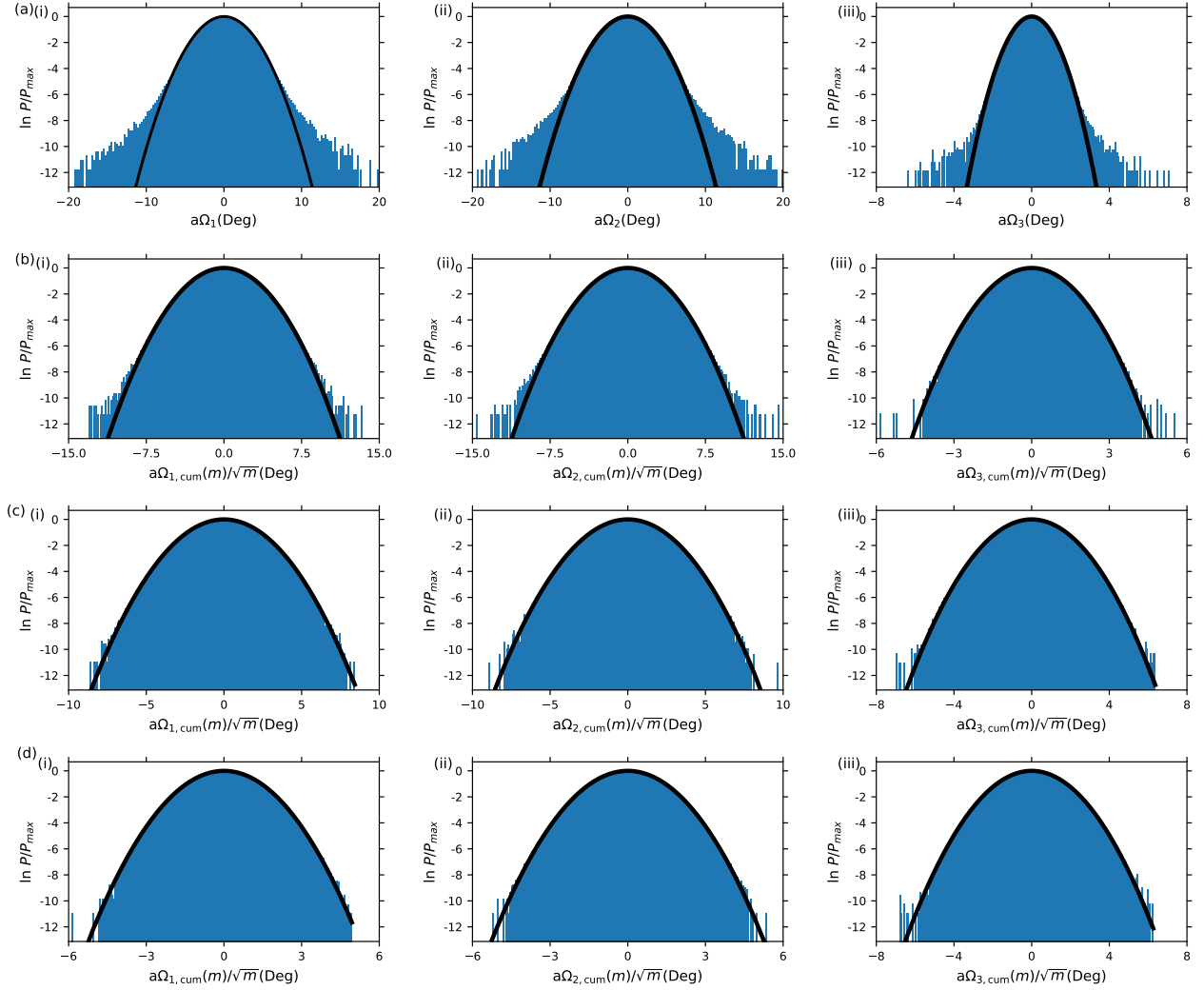


Figure S7: Probability distributions for (i)  $a\Omega_{1,\text{cum}}(m)/\sqrt{m}$ , (ii)  $a\Omega_{2,\text{cum}}(m)/\sqrt{m}$ , and (iii)  $a\Omega_{3,\text{cum}}(m)/\sqrt{m}$  for the 6HB-SST nanotube at different values of  $m$ : (a)  $m = 1$ , (b)  $m = 3$ , (c)  $m = 11$  and (d)  $m = 41$ . The solid lines are Gaussian fits to the distributions.

### S3.2 Further effects of $\alpha$

In Fig. S8 we show plots of the  $m$ -dependent elastic moduli for example origami and SST systems at  $\alpha = 0$ , i.e. without the correction to remove the helical component of the centreline of double-stranded DNA in oxDNA. Like the plot of the  $m$ -dependent persistence length for 6HB-S in the main text (Fig. 3(d)) the bending elastic moduli for this system show strong oscillations on the length scale of the DNA pitch. By contrast, the SST systems show a smooth monotonic rise even at  $\alpha = 0$ . The reason for this is most likely because the single crossovers in these systems place fewer constraints on the relative twist of different helices. The strong correlations between the orientations of the individual helices in the origamis give an additive effect causing the helix-bundle centerlines to have a significant helical character. By contrast, the reduced local orientation correlations in the SST systems cause the helical character of the centerlines of the individual DNA helices to cancel out giving a smooth nanotube centreline.

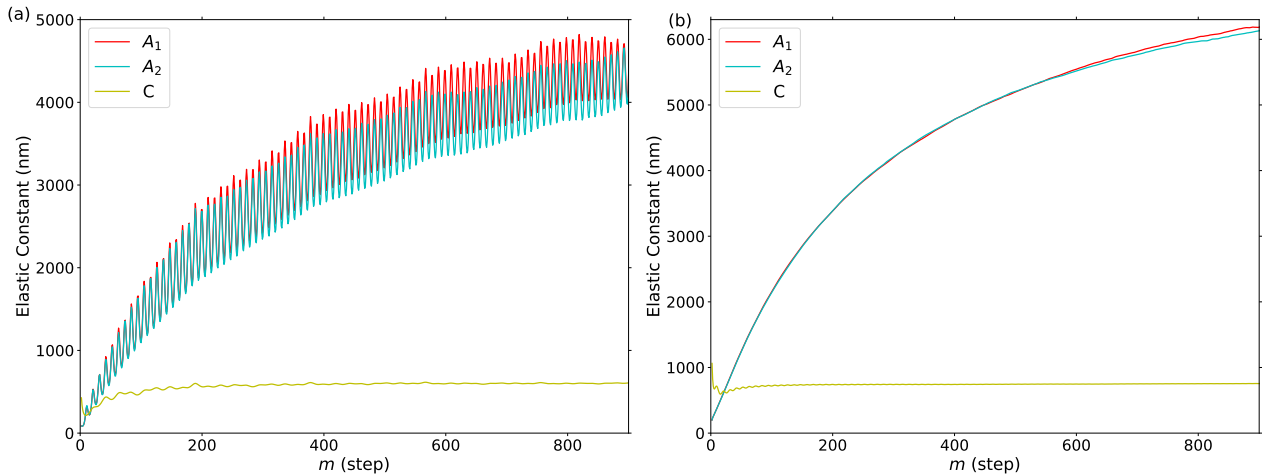


Figure S8: Elastic moduli for (a) 6HB-S and (b) 6HB-SST at  $\alpha = 0.0$ . The origami exhibits an oscillation on the pitch length of double-stranded DNA, whereas the elastic moduli increase smoothly for the SST nanotube.

The dependence of the elastic constants of double-stranded DNA on  $\alpha$  using Triad III of Ref. 56 are depicted in Fig. S9. The structural and mechanical properties of double-stranded DNA at  $\alpha = 0$ , i.e. without any correction for the helicity of the centreline, and at  $\alpha = 0.06$

Table S2: Structural and mechanical properties of double-stranded DNA before and after applying the correction to remove the helicity of the centreline. The elastic constants obtained from those at  $\alpha = 0$  by applying the transformation from a helical to a straight coordinate system outlined in Ref. 75 are also given. The results are for  $[\text{Na}^+] = 0.5 \text{ M}$  and a temperature of either  $23^\circ\text{C}$ .  $a = 0.3462 \text{ nm}$ .

	$\langle\Theta_1\rangle$	$\langle\Theta_2\rangle$	$\langle\Theta_3\rangle$	$A_1$	$A_2$	$C$	$G$	$l_b$	$l_t/2$
$\alpha = 0.00$	0.00	2.81	34.16	97.3	34.8	105.7	31.2	40.1	81.1
$\alpha = 0.06$	0.00	0.00	34.26	95.7	30.5	114.3	27.7	41.2	93.2
helically corrected				97.3	30.2	110.3	25.0		

(the value that removes the net helicity) are given in Table S2. Also included in the table are the predicted elastic constants obtained by applying a transformation from a helical to a straight coordinate system, the expressions for which were derived in Ref. 75. Comparing the two methods for removing the helicity of the centreline, the changes in  $A_2$ ,  $C$  and  $G$  are in the same direction, but with some differences in the magnitudes of the changes, and although the coordinate transformation approach predicts no change in  $A_1$ , we observe a small decrease on going from  $\alpha = 0$  to  $\alpha = 0.06$ .

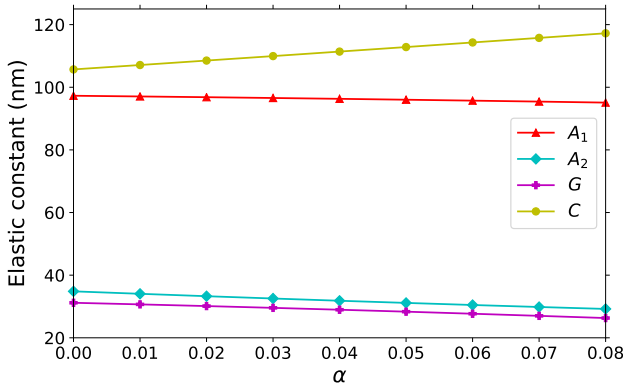


Figure S9: Double-stranded DNA elastic constants  $A_1$ ,  $A_2$ ,  $C$ ,  $G$  as a function of  $\alpha$ .

The removal of the helicity centreline makes little difference to the bending persistence length, but leads to a significant increase in the measured twist persistence length. Note also that compensating for the helicity reduces the measured pitch ( $360/\langle\Theta_3\rangle$ ) from 10.54 to 10.51 bp.

### S3.3 Triad definitions

The definitions of  $\hat{\mathbf{x}}$  and  $\hat{\mathbf{y}}$  for the six helix bundles are given in the main text, and schematically indicated in Fig. 1(d) for the other systems. Here, we give their mathematical definitions, where the numbering of the helices is as in Fig. 1(d).

For the 4HB systems:

$$\hat{\mathbf{x}} = \frac{\mathbf{R}_{\text{duplex}}(3) - \mathbf{R}_{\text{duplex}}(1)}{\|\mathbf{R}_{\text{duplex}}(3) - \mathbf{R}_{\text{duplex}}(1)\|} \quad (\text{S2})$$

and

$$\hat{\mathbf{y}} = \frac{\mathbf{R}_{\text{duplex}}(2) - \mathbf{R}_{\text{duplex}}(4)}{\|\mathbf{R}_{\text{duplex}}(2) - \mathbf{R}_{\text{duplex}}(4)\|}. \quad (\text{S3})$$

For the 8HB systems:

$$\hat{\mathbf{x}} = \frac{\mathbf{R}_{\text{duplex}}(5) - \mathbf{R}_{\text{duplex}}(1)}{\|\mathbf{R}_{\text{duplex}}(5) - \mathbf{R}_{\text{duplex}}(1)\|} \quad (\text{S4})$$

and

$$\hat{\mathbf{y}} = \frac{\mathbf{R}_{\text{duplex}}(3) - \mathbf{R}_{\text{duplex}}(7)}{\|\mathbf{R}_{\text{duplex}}(3) - \mathbf{R}_{\text{duplex}}(7)\|}. \quad (\text{S5})$$

For the 10HB system

$$\hat{\mathbf{x}} = \frac{\mathbf{R}_{\text{duplex}}(5) + \mathbf{R}_{\text{duplex}}(7) - \mathbf{R}_{\text{duplex}}(2) - \mathbf{R}_{\text{duplex}}(10)}{\|\mathbf{R}_{\text{duplex}}(5) + \mathbf{R}_{\text{duplex}}(7) - \mathbf{R}_{\text{duplex}}(2) - \mathbf{R}_{\text{duplex}}(10)\|} \quad (\text{S6})$$

and

$$\hat{\mathbf{y}} = \frac{\mathbf{R}_{\text{duplex}}(3) + \mathbf{R}_{\text{duplex}}(4) - \mathbf{R}_{\text{duplex}}(8) - \mathbf{R}_{\text{duplex}}(9)}{\|\mathbf{R}_{\text{duplex}}(3) + \mathbf{R}_{\text{duplex}}(4) - \mathbf{R}_{\text{duplex}}(8) - \mathbf{R}_{\text{duplex}}(9)\|}. \quad (\text{S7})$$

Figure S10 shows the effect of the orthogonalization scheme on the elastic moduli. If  $\hat{\mathbf{e}}_2$  is obtained by the orthogonalization of  $\hat{\mathbf{y}}$  to  $\hat{\mathbf{e}}_3$ , and  $\hat{\mathbf{e}}_1$  from the vector product of  $\hat{\mathbf{e}}_2$  and  $\hat{\mathbf{e}}_3$  (as in Triad III of Ref. 56), then  $A_1 > A_2$  for the 6HB-SST system. By contrast, if  $\hat{\mathbf{e}}_1$  is obtained by the orthogonalization of  $\hat{\mathbf{x}}$  to  $\hat{\mathbf{e}}_3$ , and  $\hat{\mathbf{e}}_2$  from the vector product of  $\hat{\mathbf{e}}_3$  and  $\hat{\mathbf{e}}_1$ , then  $A_2 > A_1$ . These results shows the biases introduced by these orthogonalization schemes. Applying the singular value decomposition technique to find the triad avoids these problems, and results in virtually equal values of  $A_1$  and  $A_2$  (Fig. 4), as is expected from the

symmetry of this system.

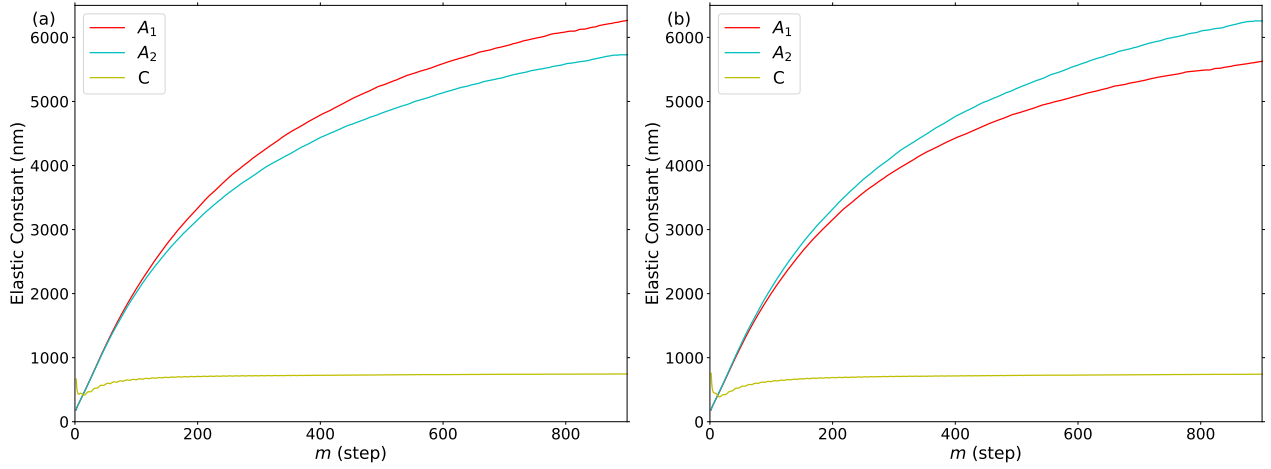


Figure S10: The effect of the orthogonalization scheme to obtain the triad  $\{\hat{\mathbf{e}}_1, \hat{\mathbf{e}}_2, \hat{\mathbf{e}}_3\}$  on the elastic moduli for the 6HB-SST nanotube. In (a)  $\hat{\mathbf{y}}$  is orthogonalized to  $\hat{\mathbf{e}}_3$ , whereas in (b)  $\hat{\mathbf{x}}$  is orthogonalized to  $\hat{\mathbf{e}}_3$ .

### S3.4 Limiting values

Fig. S11 illustrates the behaviour of the correlation function used to obtain the twist persistence length (Eq. 6) for the 6HB-SST system. It has a clear exponential tail making it straightforward to extract a limiting value of the twist persistence length. Moreover, unlike for the tangent-tangent correlation function, the deviations from exponential behaviour at small  $m$  are barely noticeable. Consequently, the  $m$ -dependent twist persistence lengths quickly converge to their limiting values.

The elastic moduli can be calculated from the correlation coefficients describing the correlations between angular deformations separated by  $n$  steps (Eq. 19) using the expression in Eq. 20. The resulting values provide a good description of the elastic moduli over the range of  $m$  sampled in simulations (Fig. S12). However, when one tries to extrapolate the predicted elastic constants to their limiting values, the results become sensitive to the statistical noise in the values of the correlation coefficients.

In Fig. 5 of the main text, we illustrate the effect of the ‘‘averaging’’ approach we use to



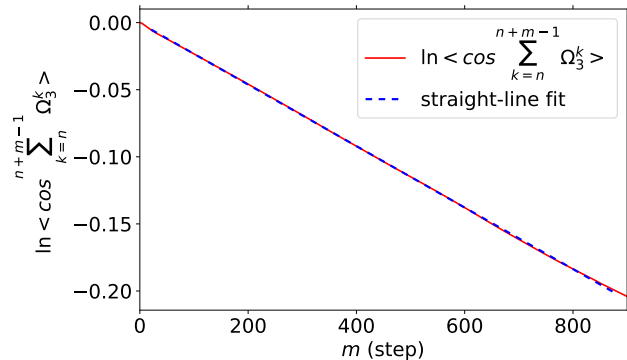


Figure S11: The exponential decay of the correlation function used to calculate the twist persistence length for the 6HB-SST nanotube.

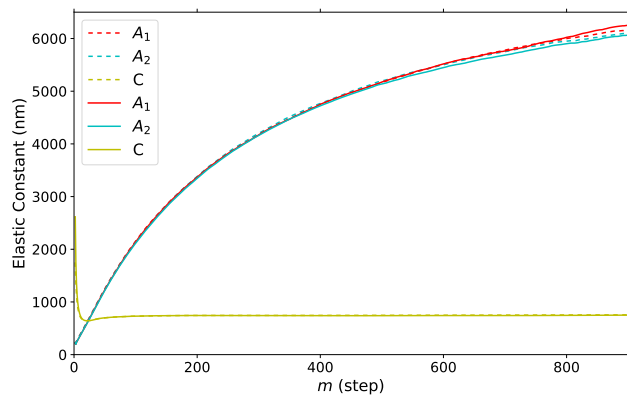


Figure S12: A comparison of elastic constants calculated using Equations 7 (solid lines) and 20 (dashed lines) for the 6HB-SST nanotube.

obtain the limiting values of the elastic constants for  $A_1$ . Equivalent figures for  $A_2$  and  $C$  are given in Fig. S13. The dependence of the behaviour on the parameter  $n_{\text{avg}}$  for  $A_2$  is, unsurprisingly, very similar to that for  $A_1$ , and except for the 10HB origami, which has the largest  $A_1/A_2$  ratio, we always use the same value of  $n_{\text{avg}}$  when computing the limiting values of these two elastic constants (Table S1). Performing this averaging is not so important for the twist elastic constant as it converges reasonably rapidly to its limiting value. This can be accelerated somewhat by using a small value of  $n_{\text{avg}}$ ; we always use  $n_{\text{avg}} = 5$ . Although we do not use this averaging approach to obtain limiting values of the persistence lengths, Fig. S13 also illustrates its effects on the  $m$ -dependent persistence lengths. Notably, the effect on the convergence of the bend persistence length is less pronounced than it is for the bending moduli.

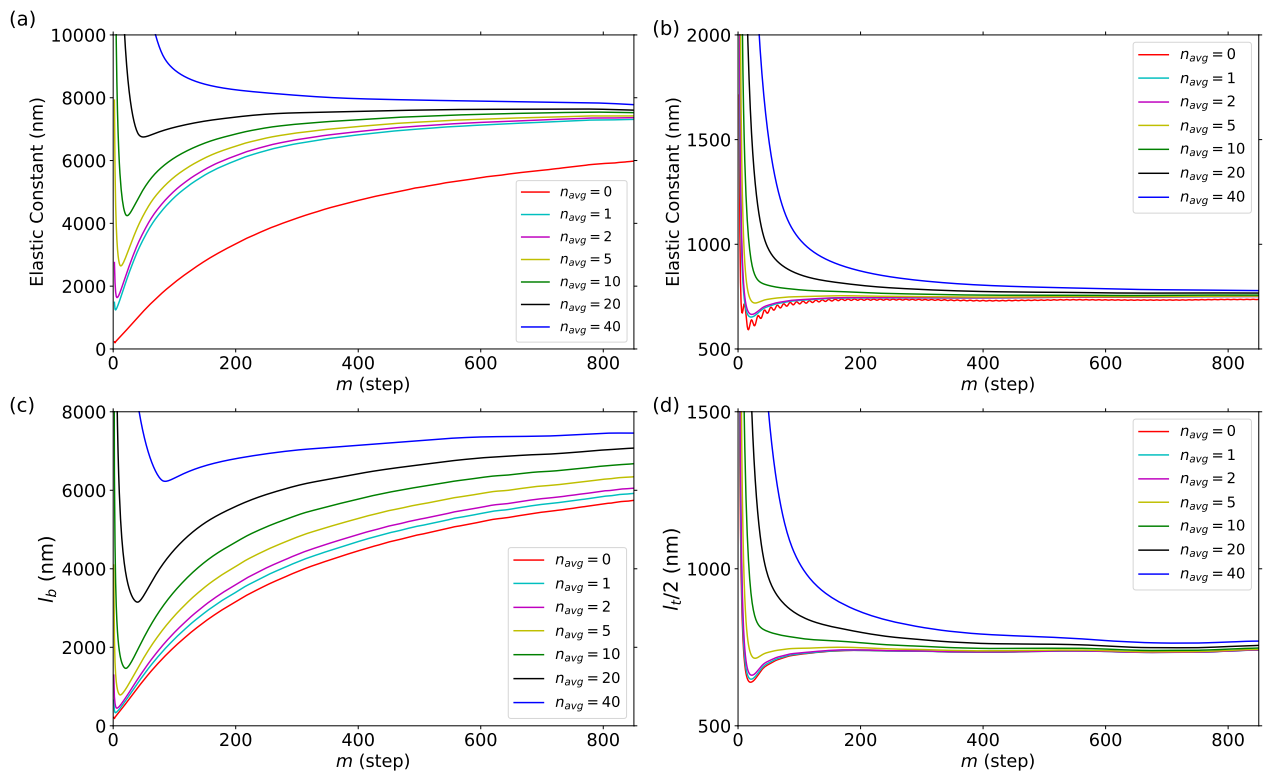


Figure S13: The effect of averaging on (a)  $A_2$ , (b)  $C$ , (c)  $l_b$  and (d)  $l_t$  for different  $n_{\text{avg}}$  for the 6HB-SST nanotube.

## S4 Further results

Fig. S14 depicts the equilibrium twist of the series of twisted origamis versus their designed twist. There is an almost perfect linear relationship, albeit with the origami that is designed to be untwisted having a small right-handed twist. Note that the oxDNA model has been fitted to reproduce the reported zero twist of an origami in Ref. 20. Interestingly, our slope is larger than would be expected from the designed twist, which is derived from the predictions of the CanDo model.<sup>50,51</sup>

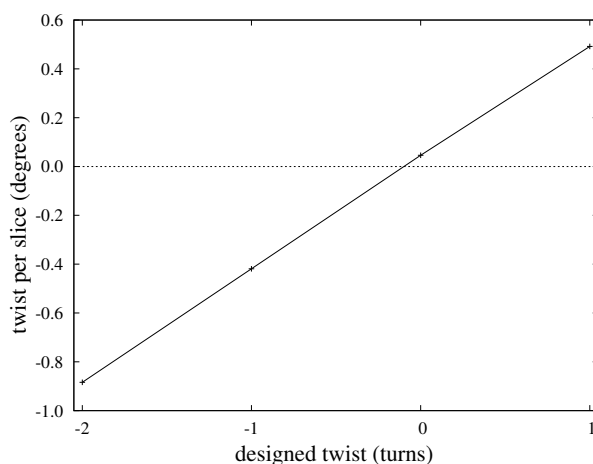


Figure S14: Twist per slice as a function of the designed twist in turns (i.e.  $2\times\text{LH}$  is  $-2$ ,  $1\times\text{RH}$  is  $+1$ ) for the series of twisted 6HB origamis.

### S4.1 Nanotube radii

The radii of the nanotubes are depicted in Figs. S15-S17 as a function of position along the tube. Note that we do not provide any results for 10HB due to its non-tubular cross-section. The periodicity seen in these plots for the main bodies of the nanotubes reflects the periodicity of the pattern of junctions. The SST tubes have a 21-slice repeat and only show very small variation in the radius, probably because their single-crossover junctions do not constrain the helices to come quite so close together as the double-crossover junctions in the origamis. The MT origamis have a clear pattern with a periodicity of 63 slices for 4HB-MT and 42 slices for 6HB-MT. The twisted tubes, by contrast, have a much more irregular

pattern of junctions and a more noisy variation in the radius, but there is still a rough repeating pattern on the order of 190 slices (modulated by the insertions and deletions). In the case of the origamis, these periodicities can be related to the small features seen in the  $m$ -dependent persistence lengths and elastic moduli at multiples of the repeat.

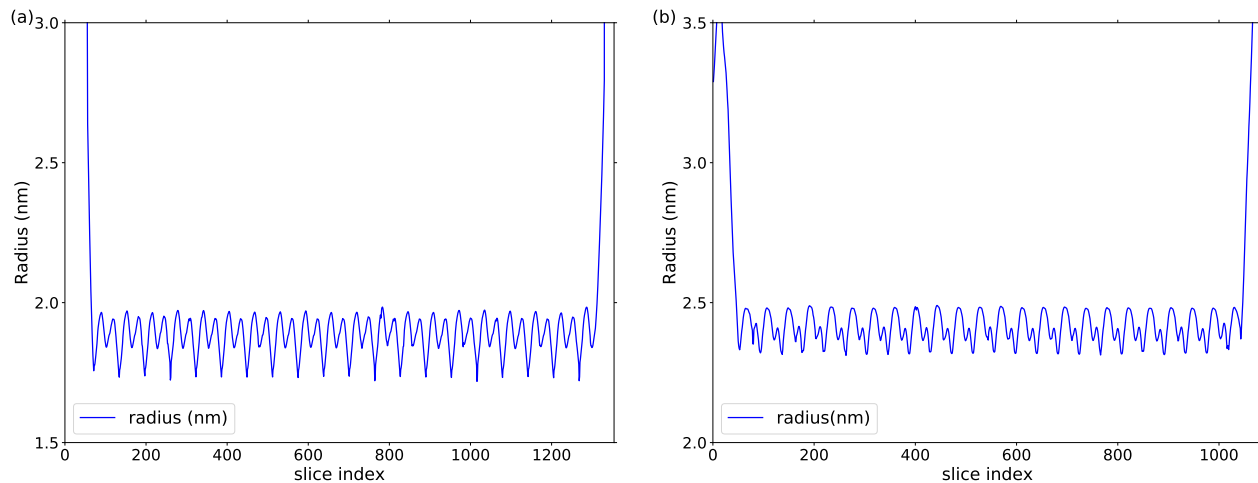


Figure S15: Radii as a function of position in the nanotube for (a) 4HB-MT and (b) 6HB-MT.

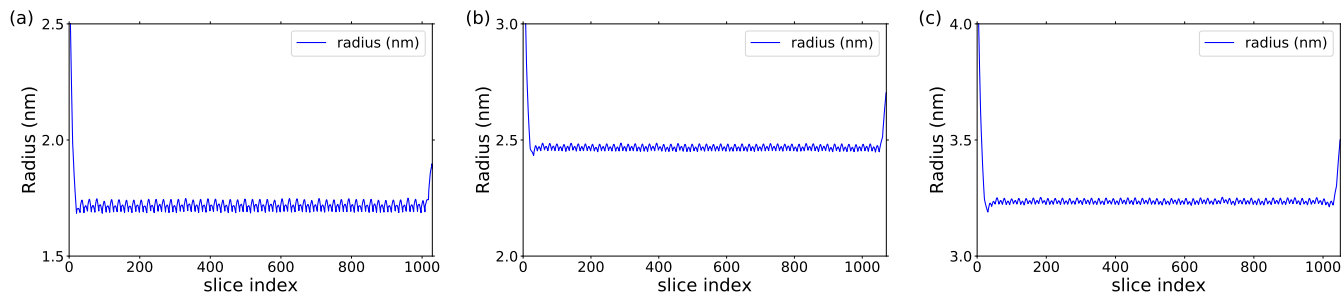


Figure S16: Radii as a function of position in the nanotube for (a) 4HB-SST, (b) 6HB-SST and (c) 8HB-SST.

## S4.2 Persistence lengths

For the SST series of nanotubes, we can compare the persistence lengths to theoretical expectations. A common approach is as follows. For a uniform elastic medium, the persistence

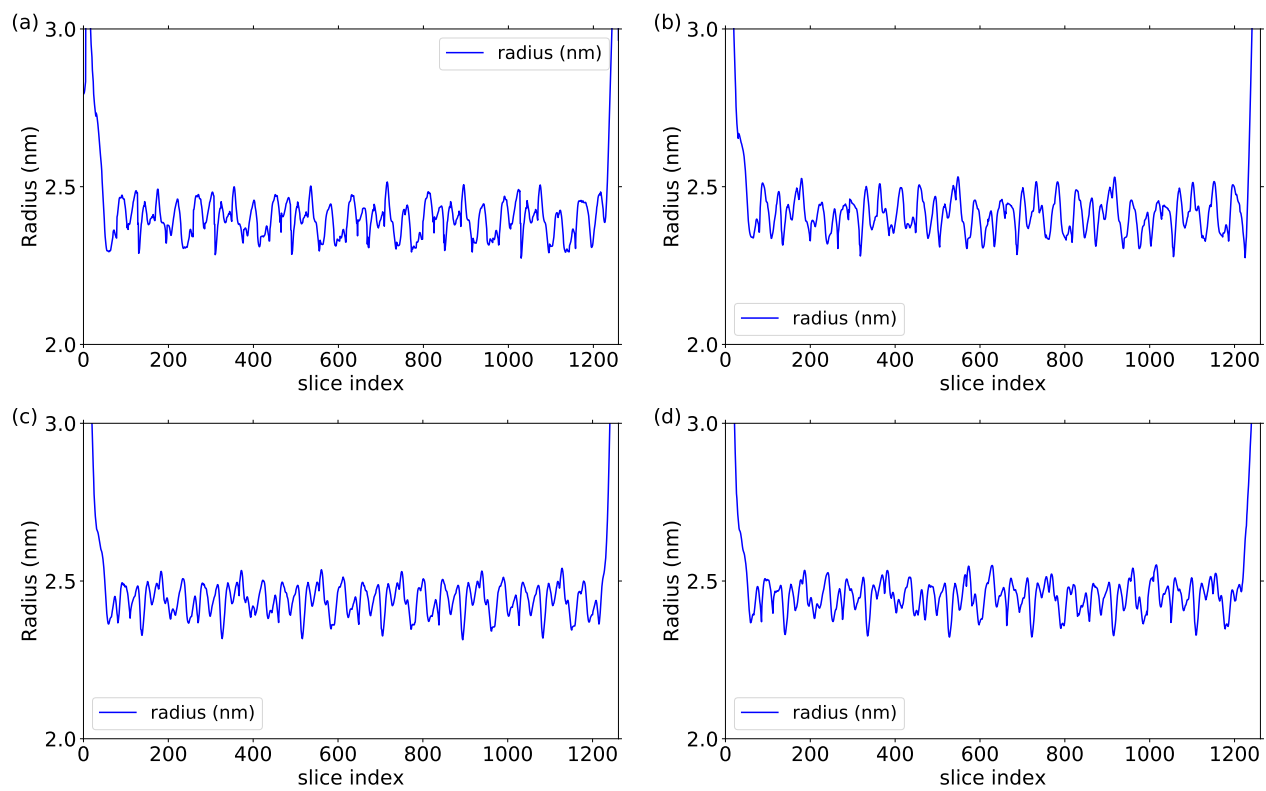


Figure S17: Radii as a function of position in the nanotube for (a) 6HB-2 $\times$ LH, (b) 6HB-1 $\times$ LH, (c) 6HB-S and (d) 6HB-1 $\times$ RH.

length can be related to the Young’s modulus through

$$l_b = \frac{YI}{k_B T} \tag{S8}$$

where  $I$  is the moment of inertia of the cross-section. Using the parallel-axis theorem to calculate  $I$  for a bundle of rods and assuming the Young’s modulus for DNA is the same in a duplex and in a helix-bundle, one arrives at the following relationship between the persistence length of a helix bundle and that for duplex DNA:

$$l_b^{\text{tube}} = n l_b^{\text{duplex}} \left( 1 + 2 \left( \frac{R}{r} \right)^2 \right). \tag{S9}$$

where  $R$  is the radius of the bundle and  $r$  the radius of duplex DNA.<sup>35</sup> In the experimental papers where this formula has been applied<sup>21,32,33,35</sup> one difficulty is that  $R$  cannot be measured directly; therefore, one first approximation has been to assume that the helices are in direct contact.<sup>21,35</sup> By contrast, for oxDNA we can measure the tube radii (e.g. Fig. S16). Thus, together with the oxDNA duplex values of  $r = 1.15$  nm and  $l_b = 41.2$  nm (Table S2), we can use Eq. S9 to predict the nanotube persistence lengths. In the main text, we use  $r$  as an effective parameter to fit the bending persistence lengths of the SST nanotubes. Other potential causes for discrepancies that have been considered in the experimental studies are imperfections in the tubes (not relevant here) and that nicks and junctions reduce the duplex persistence length for the helices in the nanotubes.

The  $m$ -dependent persistence lengths defined through Eqs. 5 and 6 are shown in Figs. S18-S21.

### S4.3 DNA extensional modulus

We performed simulations to compute the force-extension curve of double-stranded DNA. The strand was 150-bp long and we considered the central 130-bp section. The simulations were at  $[\text{Na}^+] = 0.5$  M. Forces up to 40 pN were considered.

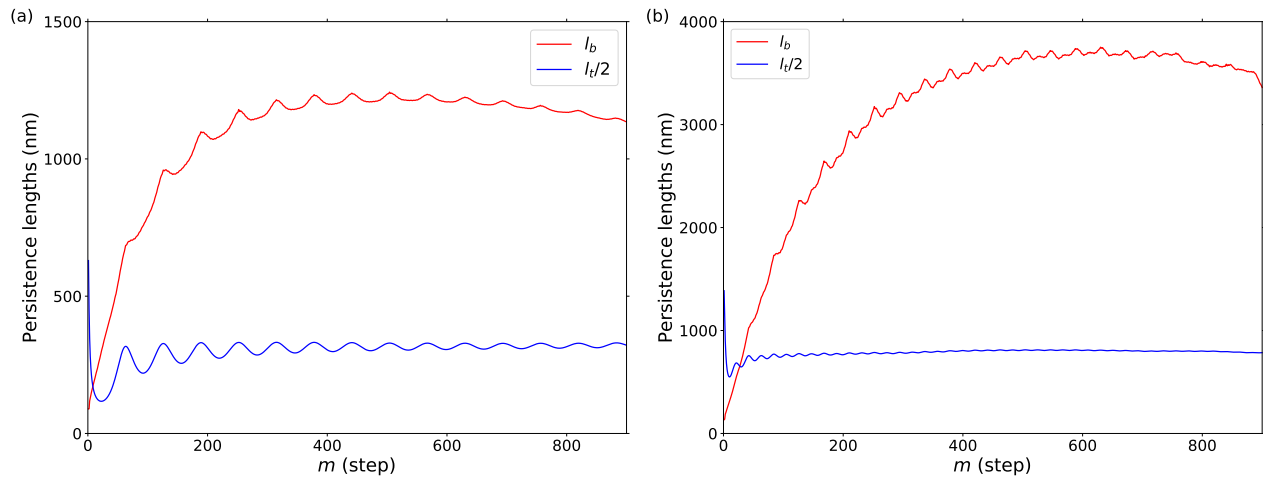


Figure S18:  $m$ -dependent persistence lengths for (a) 4HB-MT and (b) 6HB-MT.

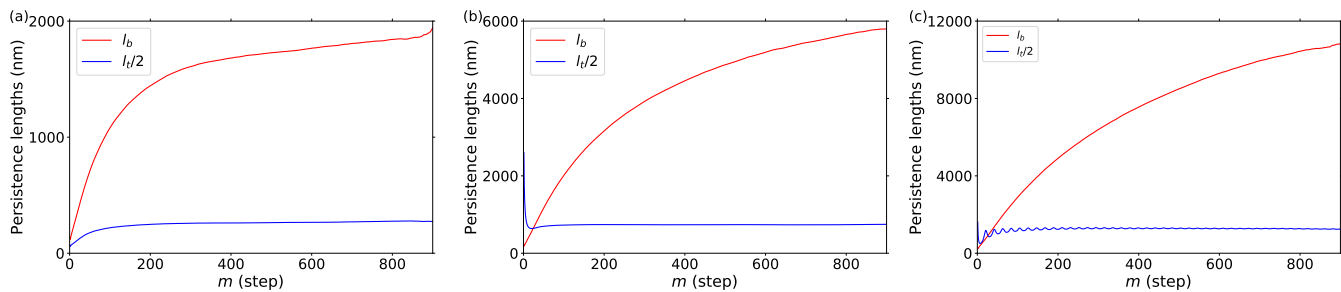


Figure S19:  $m$ -dependent persistence lengths for (a) 4HB-SST, (b) 6HB-SST and (c) 8HB-SST.

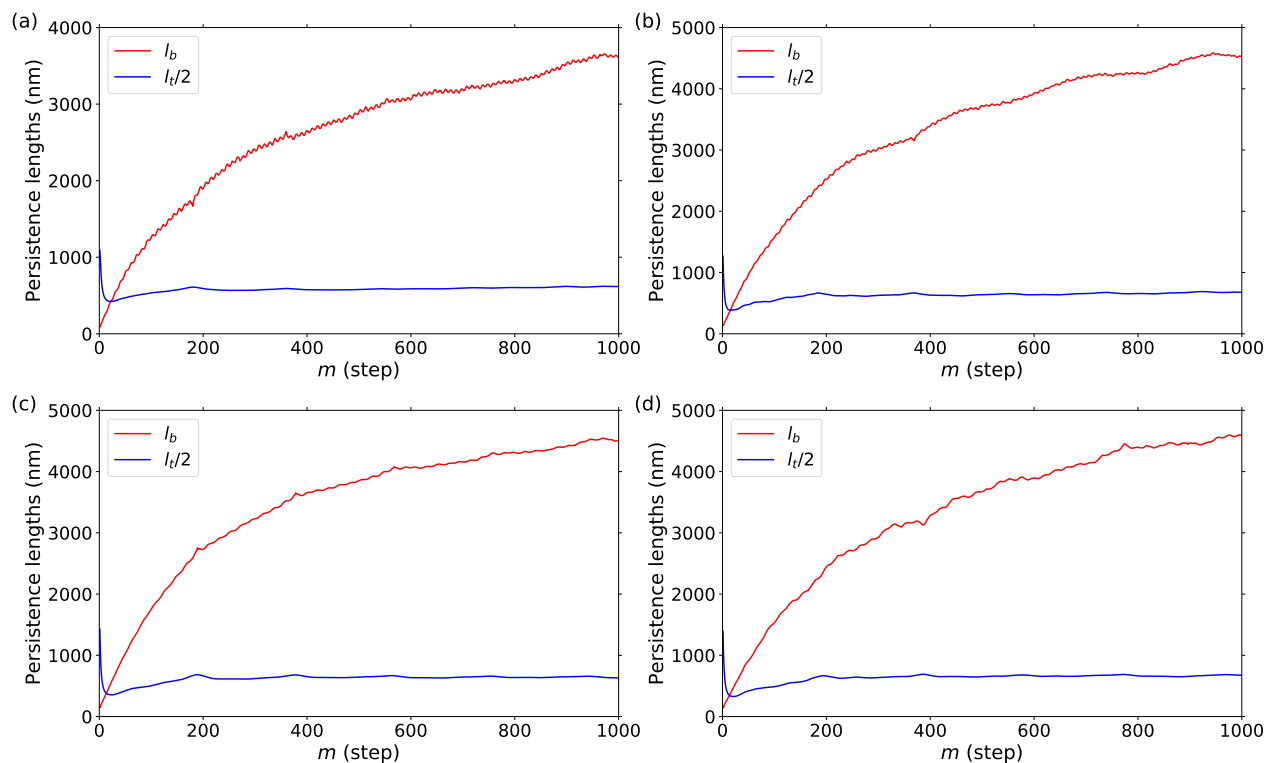


Figure S20:  $m$ -dependent persistence lengths for (a) 6HB-2 $\times$ LH, (b) 6HB-1 $\times$ LH, (c) 6HB-S and (d) 6HB-1 $\times$ RH.

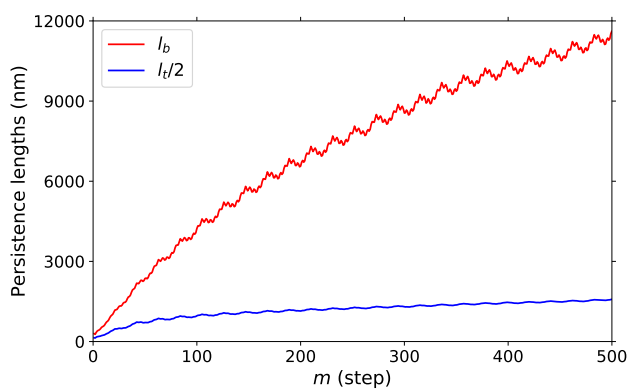


Figure S21:  $m$ -dependent persistence lengths for the 10HB origami.



The resulting data (Fig. S22) was fitted to the extensible worm-like chain expression:

$$x = L_0 \left( 1 + \frac{F}{K} - \frac{k_B T}{2FL_0} [1 + y \coth y] \right), \quad (\text{S10})$$

where

$$y = \left( \frac{FL_0^2}{l_b k_B T} \right)^{1/2}, \quad (\text{S11})$$

$L_0$  is the contour length,  $x$  is the extension,  $F$  the force and  $K$  the extensional modulus. An unconstrained three-parameter fit gave  $K = 2708$  pN,  $L_0 = 44.66$  nm and  $l_b = 49.3$  nm.

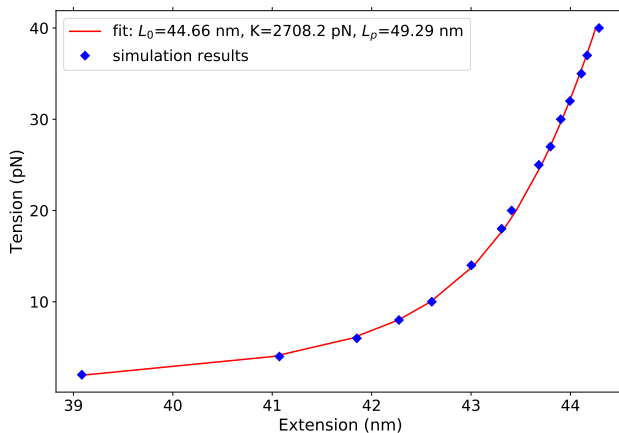


Figure S22: Force-extension curve for a 150-bp duplex, neglecting the 10 base pairs at each end. The data points are from simulations and the solid line a fit to the curve using the extensible worm-like chain formula (Eq. S10).

## S4.4 Elastic moduli

The  $m$ -dependent elastic moduli defined through Eqs. 7 and 8 are given in Figs. S23–S26. Unlike in the main text we also illustrate the off-diagonal terms. These off-diagonal terms remain closest to zero for the SST systems, which have both the best statistics and are most symmetric. For the origami systems, although these off-diagonal terms start off close to zero, there is some tendency to increase with  $m$ , particularly for  $A_{12}$ . We think this behaviour is a result of the worse statistics at longer length scales. If the off-diagonal elastic constants were actually non-zero, we would expect that their dependence on  $m$  would be

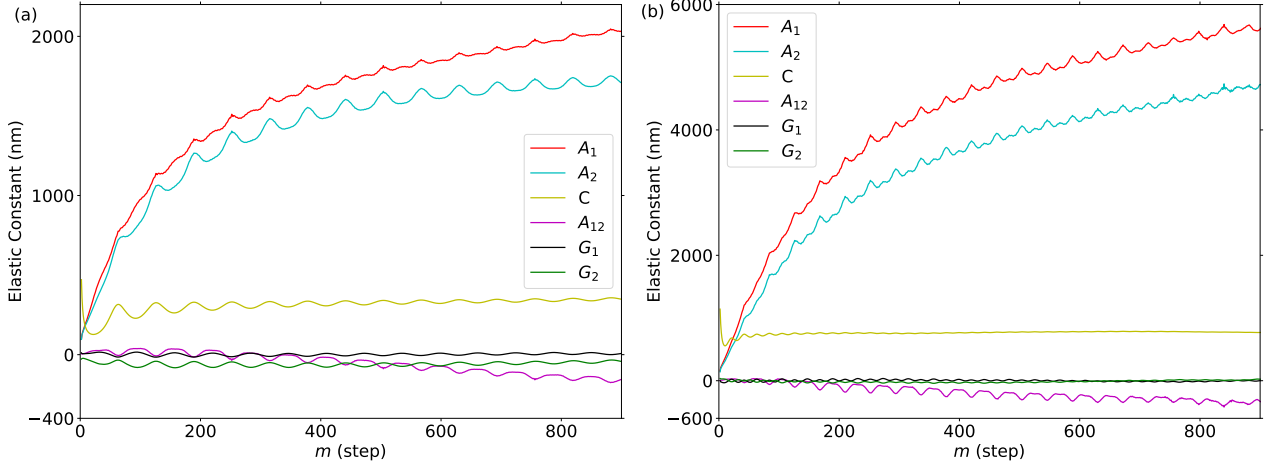


Figure S23: Elastic moduli for (a) 4HB-MT and (b) 6HB-MT.

much more similar to that for the diagonal terms, e.g. to display a monotonically decreasing slope with increasing  $m$ , as is the case for the twist-bend coupling constant for double-stranded DNA.<sup>56</sup> That  $A_{12}$  is typically the largest of the off-diagonal terms is probably due to the greater difficulty of accurately sampling bending compared to twisting, because of the much larger value of the bend persistence lengths. Unfortunately, the non-zero values of the off-diagonal terms at large  $m$  are likely to have a consequent effect on the accuracy of the limiting values of the other moduli, and to lead to deviations from the expected relationships between the persistence lengths and elastic moduli that hold when the off-diagonal terms are zero. For example, for most systems the value of  $C$  quickly converges to its limiting values and is then approximately constant for larger  $m$ . However, for the 10HB origami there is an approximately linear rise in  $C$  at large  $m$  that seems correlated with the appearance of significant deviations in  $A_{12}$  from zero (Fig. S26).

#### S4.5 SST nanotube cross-sections

In the main text we showed in Fig. 10(b) that equivalent helices in the 4HB-SST nanotube had different radii, providing quantitative evidence that the cross-section was diamond-like (Fig. 2(a)) rather than square. This is due to the inequivalence of adjacent helices in the SST nanotubes and the alternating inter-helix angle as one goes round the tube. Similar plots

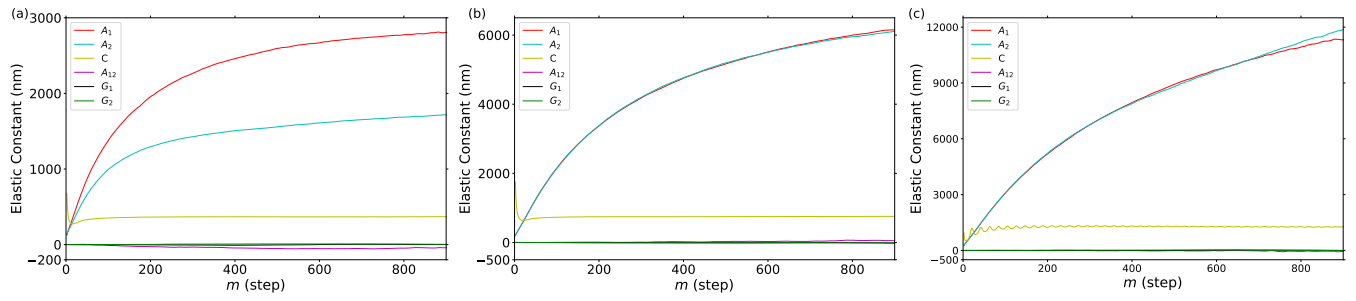


Figure S24: Elastic moduli for (a) 4HB-SST, (b) 6HB-SST and (c) 8HB-SST.

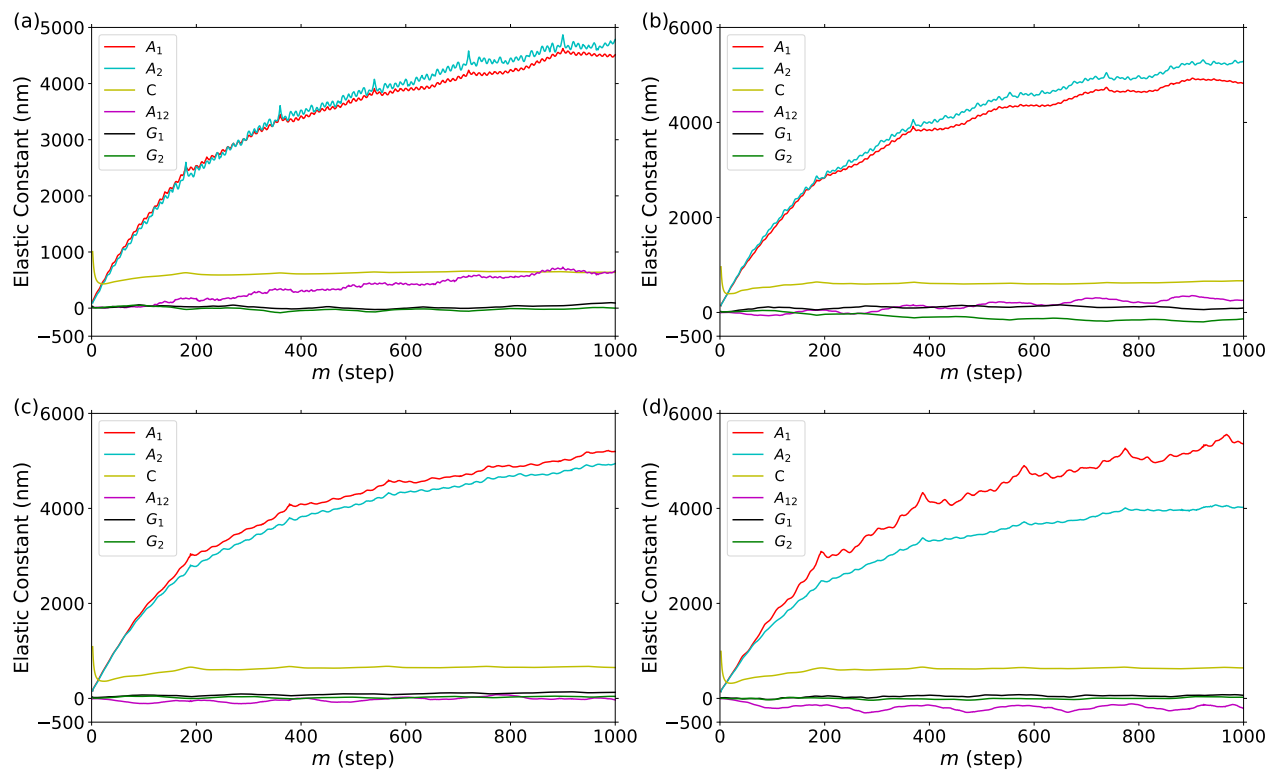


Figure S25: Elastic moduli for (a) 6HB-2xLH, (b) 6HB-1xLH, (c) 6HB-S and (d) 6HB-1xRH.

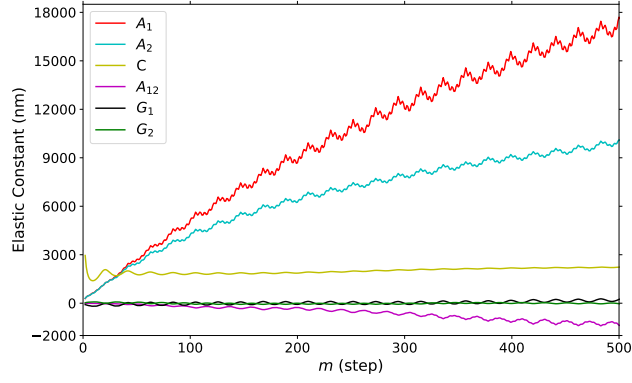


Figure S26: Elastic moduli for the 10HB origami at  $\alpha = 0.06$ .

are shown in Fig. S27 for 6HB-SST and 8HB-SST. The snapshots in Fig. S2 also confirm the deviations of the cross-section away from a regular polygon.

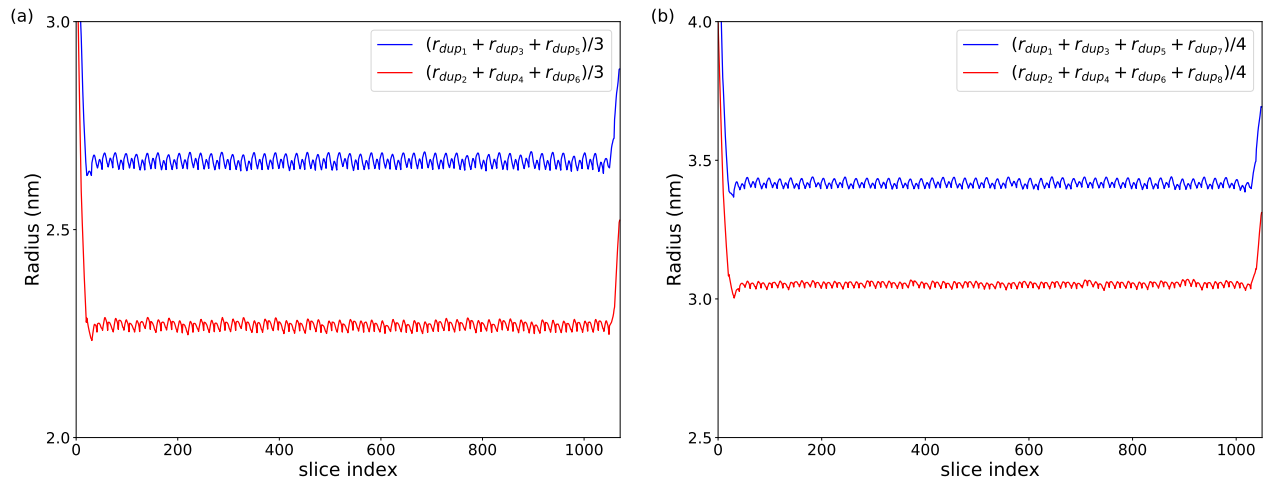


Figure S27: Radii for equivalent helices in 6HB-SST and 8HB-SST

# Graphical TOC Entry

